Biomaterials Science

ROYAL SOCIETY OF CHEMISTRY

REVIEW

View Article Online
View Journal

Cite this: DOI: 10.1039/d0bm00222d

Overview of the application of inorganic nanomaterials in cancer photothermal therapy

Natanael Fernandes,[a] Carolina F. Rodrigues,[a] André F. Moreira *[a] and Ilídio J. Correia *[a,b]

Received 10th February 2020,
Accepted 14th April 2020

DOI: 10.1039/d0bm00222d

rsc.li/biomaterials-science

Cancer photothermal therapy (PTT) has captured the attention of researchers worldwide due to its localized and trigger-activated therapeutic effect. In this field, nanomaterials capable of converting the energy of the irradiation light into heat have been showing promising results in several pre-clinical and clinical assays. Such a therapeutic modality takes advantage of the innate capacity of nanomaterials to accumulate in the tumor tissue and their capacity to interact with NIR laser irradiation to exert a therapeutic effect. Therefore, several nanostructures composed of different materials and organizations for mediating a photothermal effect have been developed. In this review, the most common inorganic nanomaterials, such as gold, carbon-based materials, tungsten, copper, molybdenum, and iron oxide, which have been explored for mediating a tumor-localized photothermal effect, are summarized. Moreover, the physicochemical parameters of nanoparticles that influence the PTT effectiveness are discussed and the recent clinical advances involving inorganic nanomaterial-mediated cancer photothermal therapy are also presented.

1. Introduction

Cancer is one of the major health problems since it is associated with high incidence and mortality rates.[1] The conventional therapies (*e.g.* surgery, chemotherapy, and radiotherapy) currently used in the clinic present several disadvantages, such as low solubility and selectivity, which hinder their therapeutic effectiveness.[2] This reality has been pushing researchers to develop new and more effective therapeutic approaches, such as immunotherapy, gene therapy, and hyperthermia.[3–5]

Hyperthermia-based cancer treatments explore the exposition of the target tissue to high temperatures that can induce the death of cancer cells (*i.e.* thermal ablation, induced by temperatures higher than 45 °C) or increase the sensitivity of cancer cells to other therapeutic modalities (mild hyperthermia, temperatures between 40 and 45 °C).[6] In conventional hyperthermia, the temperature increase in the target tissue is often achieved through outside-in approaches (*e.g.* superficial hyperthermia, regional hyperthermia, and whole-body hyperthermia based on the utilization of a thermal bath, microwaves, and radiofrequency).[7] This creates a temperature gradient that peaks in the body surface and decreases with the distance from the external heat source.[8] Therefore, the healthy tissues will also be affected by the temperature increase leading to undesired side-effects.[9]

With this in mind, researchers have been focused on the development of more efficient hyperthermia approaches, particularly those capable of inducing a localized (*i.e.* tumor confined) temperature increase.[10] In this field, nanoparticles capable of generating heat in response to outside stimuli have been used to overcome the limitations of conventional hyperthermia approaches (Fig. 1).[11] In fact, the nanoparticle size confers to them the innate capacity to accumulate on the tumor by taking advantage of the defective vasculature in the tissue (the enhanced permeability and retention effect and/or vascular bursts).[12] Then, the nanoparticles can mediate the localized thermal destruction of the cancer cells triggered by external stimuli, minimizing the damage on the surrounding healthy tissues.[13] Such features allowed the development of several nanomedicine-based hyperthermia approaches that can be classified according to the external trigger used for the activation of nanoparticles such as photothermal, magnetic hyperthermia and ultrasound hyperthermia therapies.[14–16]

Among them, the nanomaterial-mediated photothermal therapy promotes the selective death of cancer cells by irradiating the target area with laser light.[17] In the literature, several materials have already been explored to mediate this effect, such as gold, carbon, copper, tungsten, iron, and molybdenum.[18–23] Moreover, in this approach, the utilization of near-infrared (NIR) radiation is essential, particularly the

[a]CICS-UBI – Health Sciences Research Centre, Universidade da Beira Interior, Av. Infante D. Henrique, 6200-506 Covilhã, Portugal. E-mail: afmoreira@fcsaude.ubi.pt; Fax: +351 275 329 099; Tel: +351 275 329 002
[b]CIEPQF—Departamento de Engenharia Química, Universidade de Coimbra, Rua Sílvio Lima, 3030-790 Coimbra, Portugal. E-mail: icorreia@ubi.pt

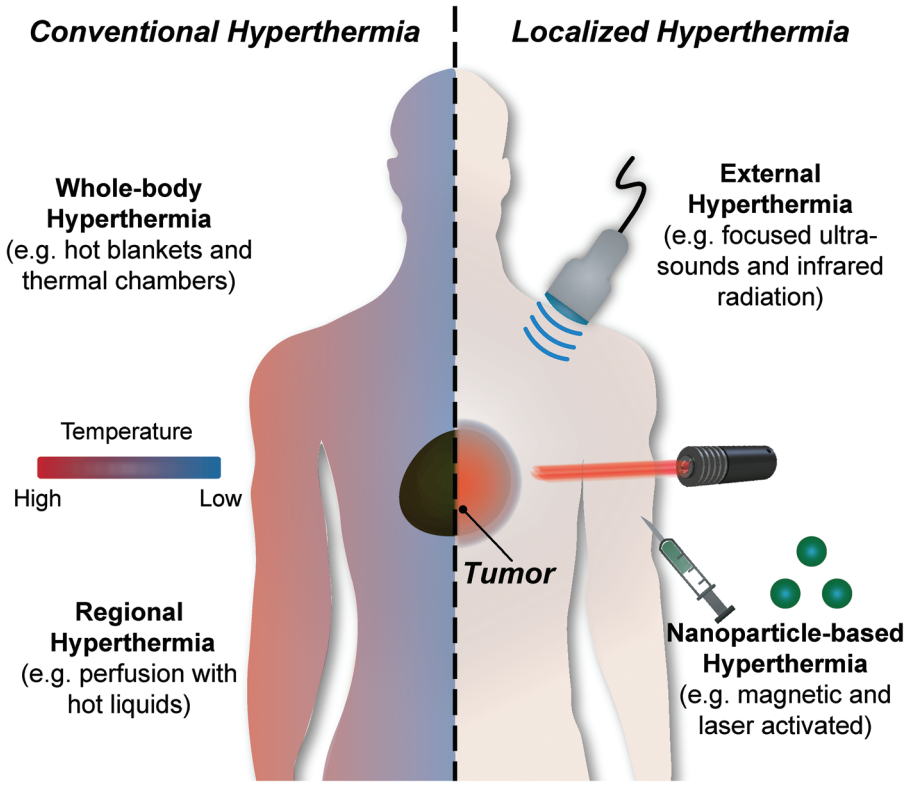

Fig. 1 Representation of the conventional and localized hyperthermia. Conventional hyperthermia creates a heat gradient from the surface region of the body to the interior. The localized hyperthermia approaches promote the specific heating of the tumor tissue, avoiding damage in the surrounding areas.

NIR-I and NIR-II radiation, since the major biological components (*e.g.* proteins, melanin, hemoglobin, collagen, and water) present minimal or insignificant absorption in this region of the spectra.[24,25] In this way, the utilization of radiation in the 750–1200 nm region guarantees the reduction of the off-target interactions and the maximum penetration in the human body, enhancing the therapeutic outcome.[17]

In this review, the most common inorganic nanomaterials explored for cancer photothermal therapy are presented, summarizing the parameters affecting the photothermal capacity. Furthermore, practical examples of their application in cancer therapy and the clinical advances based on the inorganic nanomaterial-mediated cancer PTT exploring both NIR-I and NIR-II stimuli are also presented.

2. Nanoparticle-mediated photothermal therapy

2.1. General properties

The nanomaterial cancer PTT involves the irradiation of a specific area with a NIR laser that leads to the activation of the nanostructures accumulated within the tumor.[26] Then, the local conversion of the NIR laser energy into heat mediated by nanoparticles induces a localized hyperthermia effect.[27] Therefore, the tumor selectivity of the nanomaterials is essential for PTT effectiveness.[28] The accumulation of the nanoparticles in the tumor tissue can occur through passive or active targeting phenomena.[29] The passive targeting arises due to the high proliferative rate of cancer cells, leading to the formation of defective vascular capillaries with fenestration sizes greater than 200 nm, and lymphatic vessels.[30] This abnormal vasculature facilitates the extravasation and retention of the nanoparticles in the tumor tissue.[31] Furthermore, more recently, it has also been described that the enhanced permeability in tumors can be the result of transient vascular bursts that allow the diffusion of blood to the tumor interstitium.[32] On active targeting, the accumulation of the nanoparticles on the tumor can be mediated by receptor–ligand or antigen–antibody interactions, which favor the interaction of the nanoparticles with the cancer cells.[33] Usually, in active targeting the nanomaterials are modified to explore the specific recognition of molecules overexpressed at the tumor site, such as the folate and biotin receptors.[34,35]

Nevertheless, independently of the process that mediates the accumulation of the nanoparticles in the tumor tissue, a prolonged blood circulation will increase the probability of the nanoparticles to accumulate/interact with the cancer cells.[36] In this way, there are several physicochemical parameters (*e.g.* nanoparticle size, surface charge, and corona) that have an impact on the nano–bio interaction and consequently on the blood circulation time (reviewed in detail in the studies in ref.

37–39). For example, the development of nanoparticles with sizes from 100 to 200 nm has been described as optimal for the intravenous administration in the human body.[12] This size range avoids the rapid clearance by the kidneys (nanoparticle size <5 nm), and the accumulation in the liver (nanoparticle size <50 nm) and spleen (nanoparticle size >200 nm), while maintaining the capacity to extravasate through the tumor fenestrae (nanoparticle size <200 nm).[31] Despite these ideal size values, Li and co-workers demonstrated that by increasing the size of gold nanoparticles (6.2, 24.3, 42.5 and 61.2 nm) a higher nanoparticle uptake by the liver and spleen (44–55 %ID g^{-1} and 30–40 %ID g^{-1}, respectively) occurred after 24 h of administration.[40] Similarly, Larsen and co-workers also observed an ≈8-fold increase in the uptake of PEGylated iron oxide nanoparticles by macrophage cells by increasing the size from 20 to 40 nm.[41] Moreover, Liu *et al.* reported that PEGylated gold nanoparticles with a size of 30 nm present an increased tumor uptake when compared to their counterparts with 60 nm size (2.11 ± 0.64 *vs.* 0.88 ± 0.46 %ID g^{-1}).[42] Additionally, Perrault and colleagues observed that PEGylated gold nanoparticles with 20 nm size presented an enhanced diffusion in the tumor interstitial space when compared to other equivalents with higher size, 60 and 100 nm.[43]

On the other hand, the nanoparticle surface charge can favor the uptake by the reticuloendothelial system (surface charge <−10 mV) and the interaction with serum proteins (surface charge >10 mV).[44] Therefore, nanoparticles with neutral surface charge (±10 mV) often present the longest circulation time.[45] Additionally, the adsorption of proteins on the surface of the nanoparticles can induce changes in the surface charge, prompt the aggregation of the particles, or even facilitate the recognition of the nanoparticles by the reticuloendothelial system.[46] This can be overcome by the introduction of hydrophilic and antifouling materials (*e.g.* polyethylene glycol (PEG) and polyoxazolines) or even self-membranes on the surface of the nanoparticles (Fig. 2).[47] Sharker and colleagues demonstrated that the functionalization of tungsten oxide nanoparticles with hyaluronic acid increased their biocompatibility even at high doses (1 mg mL^{-1}).[48] Furthermore, Xuan and coworkers reported that a gold nanoshell coating with self-macrophage membranes improved the blood circulation time and tumor accumulation from ≈1.6 to ≈7.5 %ID g^{-1}.[49]

Nonetheless, when the nanomaterials are aimed for cancer PTT applications, the initial focus of the researchers is the nanoparticle light/heat conversion efficiency. In nano-sized photothermal agents the photothermal capacity is closely related to the surface plasmon resonance (SPR) that corresponds to the light-induced resonant oscillation of the free electrons on the surface of the particles.[50] In this process, the nanomaterials can mediate the light scattering or absorption.[51] The light absorption induces the excitation of the free electrons on the surface of the particles and the subsequent relaxation of the electrons can release the absorbed energy in the form of luminescence or heat.[52] In PTT, nanoparticles with high absorption efficiency and low luminescence capacity are required to guarantee the most effective light/heat conversion. In addition, a localized temperature increase will only occur when the laser irradiation time is longer than the nanoparticle relaxation time, since for shorter irradiation times the gener-

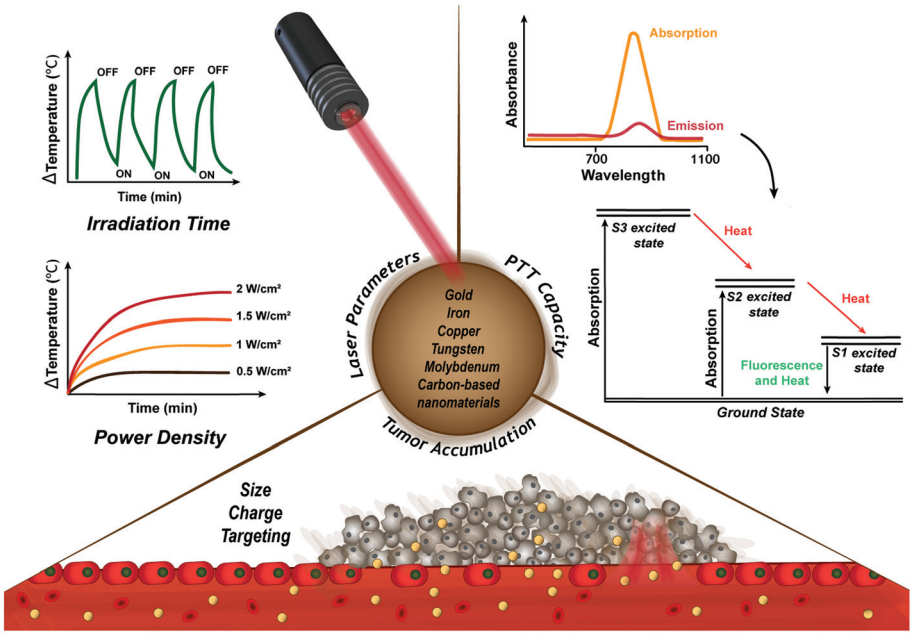

Fig. 2 Representation of the main factors that affect the PTT mediated by nanomaterials. The thermal effect induced by nanoparticles has a direct impact on their photothermal conversion efficiency (*i.e.* capacity to convert the energy absorbed into heat) and the irradiation parameters, such as the irradiation time and the power density. Furthermore, the accumulation of the nanomaterials in the tumor tissue will affect the therapeutic effectiveness.

ated heat is only confined to the nanoparticle and does not diffuse to the external medium.[9] Therefore, both the nanoparticle light/heat conversion efficiency and laser parameters (*e.g.* irradiation time and power) have to be optimized for an efficient PTT to be accomplished (reviewed in detail in the studies in ref. 11, 53 and 54). Nevertheless, it is worth noting that the NIR light can only penetrate a few centimeters in the human body, which will hinder the biological performance of the PTT mediated by nanomaterials in deep-seated tumors.[21,50] Therefore, researchers have developed different approaches to enhance the antitumoral performance of nanomaterials, such as the application of tissue implanted NIR light sources or even by combining PTT with chemotherapy, immunotherapy and photodynamic therapy.[55–58]

In the following sections, the most explored inorganic nanomaterials (such as gold, carbon-based materials, tungsten, copper, molybdenum, and iron oxide) for mediating a tumor-localized photothermal effect (Table 1) and their combination with other therapeutic approaches are described, highlighting the physicochemical parameters of nanoparticles that influence the PTT effectiveness.

2.2. Gold nanomaterials

Gold nanostructures are one of the most explored nanomaterials to mediate a photothermal effect, as already reviewed in detail in the studies in ref. 54,59 and 60. This is attributed to the localized SPR of gold nanomaterials that can mediate a strong light absorption and/or scattering.[61] These nanostructures are usually produced by promoting gold nucleation upon reduction of gold salts, using stabilizing agents to avoid nanoparticle aggregation.[62,63] Furthermore, the optimization of the synthesis process allows the tuning of the resonance wavelength to the NIR region of the spectra endowing a strong PTT capacity to the gold nanomaterials.[64] In fact, several works have already demonstrated that the PTT capacity of gold nanomaterials is dependent on the particle size, shape (*e.g.* spheres, nanorods, nanostars, and nanocages), and organization.[54,65,66]

2.2.1. Gold nanosphere-based structures. Gold nanospheres present a typical absorption band in the 500 to 550 nm region that can suffer a red-shift, on increasing the particle size.[67] Nevertheless, the gold nanosphere size increase does not allow the fine-tuning of the absorption peak to the NIR region (*i.e.* usually only up to 600 nm).[68,69] When PTT applications are envisioned, the application of gold nanospheres occurs when organized in nanosphere shells and/or clusters. The localized SPR of gold nanosphere-based shells and clusters presents a shift in the absorption peak from the visible to the NIR region of the spectra, when interparticle gaps are decreased.[70–72] This is attributed to the interparticle interactions that result in the coupling of the plasmon oscillations due to interactions of the near-field of one particle with the adjacent ones in close proximity.[73,74] Li *et al.* produced U11 targeted gold nanoclusters containing a cathepsin E sensitive PDT therapy prodrug (5-ALA) and a cyanine dye (Cy5.5) for the pancreatic ductal adenocarcinoma photothermal and photodynamic therapy.[75] For this purpose, gold spheres with a 10 nm diameter were initially modified with Cys-Arg-Gln-Ala-Gly-Phe-Ser-Leu-5-ALA (CRQAGFSL-5-ALA) and Cys-Arg-Gln-Ala-Gly-Phe-Ser-Leu-Cy5.5 (CRQAGFSL-Cy5.5). Then, the gold nanoparticles were crosslinked using 1,9-nonanedithiol (*i.e.* exploring) gold–thiol interactions to form spherical gold clusters with an ≈53 nm diameter, which were further functionalized with PEGylated U11 targeting peptides. The resulting gold nanoclusters presented a red-shift of the absorption peak of the gold spheres from 532 nm to 544 nm, as well as an increased absorption capacity in the 700–800 nm region. Additionally, the authors reported that the gold nanoclusters could mediate a temperature increase from 20 °C to around 50 °C after being irradiated with a NIR laser (750 nm, 2 W cm^{-2} for 5 min). Moreover, the U11 targeted gold nanoclusters were found to be biocompatible at concentrations as high as 5 nM (*i.e.* PANC1 CTSE cell viability was greater than 80% after 24 hours of incubation with gold nanoclusters) and showed a preferential accumulation on the tumor tissues. The authors also demonstrated that the intravenous administration of U11 targeted gold nanoclusters containing 5-ALA and Cy5.5 (2 pmol per mouse) could mediate an antimoral effect. In fact, an inhibition of the tumor growth has been reported when only PDT or PTT treatments were performed, whereas the combinatorial PDT/PTT treatment resulted in the almost complete eradication of the tumors, after 15 days. In a similar approach, Park and colleagues produced albumin nanoparticles containing gold nanoclusters and Cy5.5 for cancer fluorescence imaging and PTT.[76] The particles were produced by mixing the gold nanospheres (≈4.4 nm in diameter) with different amounts of albumin in order to promote their agglomeration. A close entrapment of the gold nanospheres on the albumin particles resulted in a greater absorbance over the 600–900 nm region. Moreover, nanoparticles formulated with 10 mg mL^{-1} of albumin were able to mediate an increase in the temperature up to 70 °C after irradiation with a NIR laser (808 nm, 1.5 W cm^{-2} for 10 min). Additionally, the *in vivo* assays demonstrated that the intravenous administration of albumin/gold nanoclusters (200 μL at 10 mg mL^{-1}) remarkably suppressed the tumor growth. A reduction of the tumor size from 150 mm^3 to 17.8 mm^3 upon NIR laser irradiation (808 nm, 1.5 W cm^{-2} for 10 min) was observed. Wang and coworkers developed gold nanoshell coated chitosan modified liposomes loaded with resveratrol for the chemo-PTT of cancer.[77] For that purpose, small-sized gold spheres were attached to the surface of chitosan modified liposomes (formation of Au–N bonds) and subsequently reacted with a growth solution (gold precursor and reducing agent). The growth solution allows the assembly of new gold atoms on the surface of the small-sized gold spheres forming large gold nanoparticles and a uniform shell at the liposome surface. The authors reported a red-shift in the absorption peak with the growth of the gold nanoparticles in the liposome surface, exhibiting a broad absorption band in the 550–800 nm region. In addition, the authors also observed that the photothermal effect generated by these nanomaterials remained constant during 5 cycles of

Table 1 Overview of the different properties of inorganic nanoparticles (gold, tungsten, molybdenum, iron oxide, copper, and carbon-based materials) for application in PTT. (W) Width; (L) length; (AR) aspect ratio; (MS) mesoporous silica; and (D) diameter

Materials	Morphology and surface modification	General properties	Absorption band	Dose	PTT			Type of cancer *in vitro*/*in vivo*	Ref.
					Laser	Temperature	PTT conversion efficiency		
Gold	Rabies virus-mimetic silica-coated gold nanorods	L: 79.9 nm; W: 20.1 nm; AR: 4; sílica shell: 13.8 nm	820 nm	0.1 mM	808 nm, 1.5 W cm^{-2} for 5 min	$T_{max} \approx 50.0$ °C	—	N2a cells/N2a tumor-bearing mice	176
	HA and RGD with MS-coated gold nanorods	L: 50 nm; W: 10 nm; silica shell: 15 nm	520 and 780 nm	40 μg mL^{-1}	808 nm; 2.0 W cm^{-2} for 4 min	$T_{max} = 43.5$ °C	—	SKOV-3 cells	177
	MS-coated gold nanorods loaded with indocyanine green, end-capped with β-cyclodextrin and RLA peptide anchored	L: 57.3 nm; W: 16.2 nm; AR: 3.47; sílica shell: 21 nm	813 nm	4.2 mg mL^{-1}	808 nm; 2.0 W cm^{-2} for 9 min	$\Delta T = 31.2$ °C	—	MCF-7 cells/ MCF-7 tumor-bearing mice	178
	MS-coated gold nanorods coated with *in situ* formed silver nanoparticles	L: 46 nm; W: 19 nm; silica shell: 15 nm	684 nm	100 μg mL^{-1}	780 nm; 3.0 W cm^{-2} for 10 min	$T_{max} = 44.6$ °C	—	HeLa and L02 cells	179
	Mesoporous silica-coated gold nanorods, β-cyclodextrin as gatekeeper functionalized with lactobionic acid and PEG	L: 39.8 nm; W: 10.2 nm; AR: ≈3.9; sílica shell: ≈14 nm	677 and 791 nm	25 and 50 μg mL^{-1}	808 nm; 0.37 and 1.01 W cm^{-2} for 8 min	$T_{max} \approx 64.8$ °C (50 μg mL^{-1} and 1.01 W cm^{-2}); $T_{max} \approx 39.1$ °C (25 μg mL^{-1} and 0.37 W cm^{-2})	—	HepG2 and COS7 cells/ HepG2 tumor-bearing mice	180
	MS coated gold nanorods capped with poly (NIPAAm-*co*-BVIm)	L: 45 nm; W: 10 nm; AR: 4.5; silica shell: ≈30 nm	850 nm	60 μg mL^{-1}	850 nm; 100.0 mW for 5 min	$T_{max} \approx 65.0$ °C	—	HeLa cells	181
	Bacteria-like mesoporous silica coated gold nanorods functionalized with PEG	L: 104.6 nm; W: 68.6 nm; AR: 3.7; silica shell: 23.5 nm	805 nm	0.5 mg mL^{-1}	808 nm; 0.25 W cm^{-2} for 10 min	$T_{max} = 45.0$ °C	29.6%	4T1 cells/4T1 tumor-bearing mice	182
	Nanostars	Size: 30 nm containing 95.5% gold and 4.5% silver; size: 60 nm containing 96.9% gold and 3.1% silver	706 nm (60 nm) and 945 nm (30 nm)	0.5 nM (30 nm)	980 nm; 0.8 W cm^{-2} for 20 min	$T_{max} \approx 42.0$ °C (30 nm)	94% (30 nm) and 90% (60 nm)	Mouse sarcoma tumor-bearing mice	42
	Gold nanostar coated hollow MS encapsulated with PFH and functionalized with PEG	Nanostar size: 60 nm; hollow MS: 200 nm	520 and 795 nm	20 mM Au concentration	808 nm; 1.2 W cm^{-2} for ≈6 min	$\Delta T = 40.2$ °C	67.1%	C6 cells/C6 tumor-bearing mice	183
	Organosilica coating onto gold nanostars with conjugation of Gd chelates and functionalized with PEG	Core: 60 nm; organosilica shell: 20 nm	800 nm	—	808 nm; 0.5 W cm^{-2} for 10 min	$T_{max} = 68.0$ °C	—	MDA-MB-231 cells/ MDA-MB-231 tumor-bearing mice	184
	Gold nanostar core, MS shell coated with FA	Core: 50 nm; silica shell: 50–60 nm; total size: ≈150 nm	≈800 nm	38.5 μg mL^{-1}	808 nm; 800 mW for 5 min	$T_{max} = 51.27$ °C	31.21%	HeLa and A549 cells/HeLa tumor-bearing mice	185

Table 1 *(Contd.)*

Materials	Morphology and surface modification	General properties	Absorption band	Dose	PTT			Type of cancer *in vitro*/*in vivo*	Ref.
					Laser	Temperature	PTT conversion efficiency		
	Polydopamine coated gold nanostars stabilized with PEI	D: 74.2 nm; silica shell: 18 nm	726 nm	0.35 mM Au concentration	808 nm; 1.3 W cm^{-2} for 5 min	ΔT = 15.1 °C	40%	HeLa cells/HeLa tumor-bearing mice	186
	RGD-modified dendrimer stabilized-gold nanostars	Total size: 55.1 nm	800 nm	20 mM	808 nm; 1.2 W cm^{-2} for 5 min	ΔT = 55.0 °C	79%	U87MG cells/ U87MG tumor-bearing mice	187
	Gold nanoshell-coated liposomes containing betulinic acid	Size of the liposomes: 149.4 nm	550–900 nm	58 μg mL^{-1}	808 nm; 2.0 W cm^{-2} for 10 min	T_{max} = 43 °C	—	143B and HeLa cells/U14 tumor-bearing mice	188
	Anti-epidermal growth factor receptor antibody-conjugated and paclitaxel loaded-thiol chitosan-layered gold nanoshells	Silica core: 120 nm; gold nanoshell: 9 nm	700–900 nm	175 μg mL^{-1}	808 nm; 1.2 W cm^{-2} for 5 min	$T_{max} \approx$ 52.5 °C	32.63%	HeLa and MDA-MB231 cells/ MDA-MB231 tumor-bearing mice	78
	Gold nanoshells onto the silica nanoparticles with dendrimer porphyrin and functionalized with PEI	Size: 186.2 nm	N.D.	—	808 nm; 2.0 W cm^{-2} for 5 min	$T_{max} \approx$ 62.0 °C	—	HeLa cells	189
	Macrophage cell membrane camouflaged gold nanoshell coated MS nanoparticles	Gold nanoshell: 12 nm; MS: 80 nm; macrophage membrane: 200 nm	810 nm	1 mg mL^{-1}	808 nm; 1.0 W cm^{-2} for 5 min	ΔT = 30.0 °C	—	4T1 cells/4T1 tumor-bearing mice	49
	Nanoclusters made from ultra-small gold nanoparticles encapsulated into larger spherical polymeric nanoconstructs of PLGA core stabilized by PEG	Ultra-small nanoparticles: 6 nm; size: 100–180 nm	520 nm	200 μg mL^{-1}	800 nm; 100 J cm^{-2} for 1 min	ΔT = 20.0 °C	—	SUM-159 and U87-MG cells	190
	Gold nanocluster-loaded hybrid albumin nanoparticles	Agglomeration of gold nanoparticles with an average size of 4.4 nm	600–900 nm	10 mg mL^{-1}	808 nm; 1.5 W cm^{-2} for 10 min	$T_{max} \approx$ 70.0 °C	—	HCT 116 cells/ HCT 116 tumor-bearing mice	76
	Core gold nanocage shell MS	Ag nanocube L: ≈60 nm; condensed silica layer: ≈8 nm; MS: ≈25 nm; total size: 130 nm	530 nm	50 μg mL^{-1}	808 nm; 1.0 W cm^{-2} for 10 min	ΔT = 16.0 °C	—	HeLa cells	191
	Double-walled gold nanocage/silica nanorattles	Ag nanocube: ≈35 nm; gold wall: ≈4 nm; silica layer: 45 nm; average size: 120–130 nm	789 nm	1.20 mg mL^{-1}	808 nm, 123.8 mW cm^{-2} for 10 min	ΔT = 15.3 °C	—	MCF-7 cells	192
	MicroRNA-181b into PEI-modified and FR-targeted PEGylated gold nanocages	Gold nanocube: 50 nm; total size: 170.6 ± 4.2 nm	802 nm	9.7 μg mL^{-1}	808 nm; 1.25 W cm^{-2} for 10 min	ΔT = 28.2 °C	—	SMMC-7721 cells/SMMC-7721 tumor-bearing mice	90

Table 1 *(Contd.)*

Materials	Morphology and surface modification	General properties	Absorption band	Dose	PTT			Type of cancer *in vitro*/*in vivo*	Ref.
					Laser	Temperature	PTT conversion efficiency		
Tungsten	WO_{3-x}@γ-poly-L-glutamic acid nanoparticles	Size: 5.75 nm	N.D.	200 mg mL^{-1}	1064 nm; 0.5 W cm^{-2} for 10 min	ΔT = 22.3 °C	25.8%	HUVEC and 4T1 cells/4T1 tumor-bearing mice	137
	Dopamine-conjugated HA encapsulating coated WO_3	Size: 176.25 nm	800–1100 nm	1 mg mL^{-1}	808 nm; 2.0 W cm^{-2} for 5 min	T_{max} = 44.0 °C	11.78%	MDAMB-231/ MDAMB-231 tumor-bearing mice	48
	$W_{18}O_{49}$ nanoparticles with integrin-targeting peptide iRGD and HSP90-inhibitor 17AAG	$W_{18}O_{49}$ nanoparticle size: 10 nm; total size: 120 nm	600–1000	100 μg mL^{-1}	808 nm; 2.0 W cm^{-2} for 5 min	ΔT = 21.8 °C	—	MKN-45P cells/ MKN-45P tumor-bearing mice	136
	Platelet membranes as nanocarriers to co-load $W_{18}O_{49}$ nanoparticles	$W_{18}O_{49}$ nanoparticle size: 5 nm; size: 115 nm	600–1200	1 mg tungsten per ml	808 nm; 1.0 W cm^{-2} for 10 min	ΔT = 37.4 °C	—	PBMCs and Raji cells/Raji lymphoma bearing mice	135
	$(NH_4)_xWO_3$ nanorods functionalized with PEG	W: 100 nm; L: 0.5–1.0 μm	800–1200 nm	400 μg ml^{-1}	808 nm; 2.0 W cm^{-2} for 3 min	ΔT = 40.0 °C	32.7%	SUM-159 and MCF-7 cells	193
	Lentinan decorated $W_{18}O_{49}$ nanorods	W: 40 nm; L: 180 nm; lentinan layer: 10 nm	650–1200 nm	125 μg mL^{-1}	980 nm; 0.4 W cm^{-2} for −13 min	ΔT = 15.1 °C	33.86%	MDA-MB231 cells	140
	Cs_xWO_3 nanorod coated with polyelectrolyte ultilayers	W: 26 nm; L: 85 nm	780–2500 nm	0.5 mg mL^{-1}	880 or 1064 nm; 2.0 W cm^{-2} for 10 min	$\Delta T \approx$ 30.0 °C (880 nm); $\Delta T \approx$ 35.0 °C (1064 nm)	—	HeLa and L02 cells/HeLa tumor-bearing mice	133
	WS_2 nanosheets functionalized with PEG	Size: 50–100 nm; thickness: ≈1.6 nm	N.D.	0.5 mg mL^{-1}	808 nm; 0.8 W cm^{-2} for 5 min	$\Delta T \approx$ 65.0 °C	—	4T1, HeLa and 293T cells/4T1 tumor-bearing mice	194
	BSA exfoliated WSe_2 nanosheets	Size: 100–200 nm; thickness: 4–5 nm	N.D.	1.0 mg mL^{-1}	808 nm; 3.6 W cm^{-2} for 5 min	ΔT = 25.0 °C	35.07%	HeLa cells/U14 tumor-bearing mice	195
	BSA coated WS_2 nanosheets	Size: 20–100 nm; thickness: 4–5 nm	N.D.	450 μg mL^{-1}	808 nm; 1.0 W cm^{-2} for 10 min	ΔT = 30.0 °C	32.83%	HeLa cells/HeLa tumor-bearing mice	196
	WS_2 quantum dots	Size: 3 nm	N.D.	100 μg mL^{-1}	808 nm; 1.0 W cm^{-2} for 10 min	ΔT = 20.0 °C	44.3%	HeLa and HepG 2 cells/BEL-7402 tumor-bearing mice	197
Molybdenum	MoO_2 nanoparticles	Size: ≈10.5 nm	795 nm	80 μg mL^{-1}	808 nm; 2.0 W cm^{-2} for 10 min	T_{max} = 73.5 °C	61.3%	Hep G2 cells	146
	MoO_x nanoparticles functionalized with PEG	Size: 15–30 nm	410 nm	200 μg mL^{-1}	808 and 1064 nm; 1.0 W cm^{-2} for 10 min	ΔT = 18.1 °C (808 nm); ΔT = 29.5 °C (1064 nm)	27.3% (808 nm); 37.4% (1064 nm)	HeLa, HepG2 and PANC-1/ PANC-1 tumor-bearing mice	142
	Mo_2C nanospheres	Size: 50 nm composed of crystals of 2–4 nm	N.D.	1 mg mL^{-1}	1064 nm; 2.0 W cm^{-2} for 10 min	$T_{max} \approx$ 62.0 °C	24.95%	HepG2, HUVEC and IOSE80 cells/HepG2 tumor-bearing mice	198
	MoO_{3-x} hollow nanospheres functionalized with PEG	Size: 142 nm	700–1000 nm	0.5 mg mL^{-1}	808 nm; 1.0 W cm^{-2} for 10 min	$T_{max} \approx$ 53.0 °C	≈22.64%	Hela, MCF-7 and PANC-1 cells/ PANC-1 tumor-bearing mice	156

Table 1 *(Contd.)*

Materials	Morphology and surface modification	General properties	Absorption band	Dose	PTT			Type of cancer *in vitro*/*in vivo*	Ref.
					Laser	Temperature	PTT conversion efficiency		
	MoO_x nanosheets functionalized with PEG	Size: 90 nm; thickness: 1.5 nm	700–1000 nm	80 μg mL^{-1}	808 nm; 0.7 W cm^{-2} for 5 min	$T_{max} \approx 60.0$ °C	—	4T1/4T1 tumor-bearing mice	150
	MoO_x nanosheets functionalized with pluronic-F127	Size: 80–100 nm; thickness: 1.5 nm	≈800 nm	500 μg mL^{-1}	808 nm; 1.0 W cm^{-2} for 5 min	$\Delta T = 40.8$ °C	—	4T1 and MCF-7 cells/4T1 tumor-bearing mice	18
	MoS_2 nanosheets functionalized with PEG	Thickness: ≈1 nm	N.D.	0.06 mg mL^{-1}	808 nm; 0.7 W cm^{-2} for 5 min	$\Delta T \approx 52.0$ °C	—	4T1 cells/4T1 tumor-bearing mice	145
	MoS_2 nanosheet capped mesoporous organosilicas functionalized with PEI	Mesoporous organosilica: 196 nm; nanosheet size: 120–300 nm and thickness: 1.5–2 nm	255 nm	2 mg mL^{-1}	808 nm; 1.0 W cm^{-2} for 5 min	$T_{max} = 53.7$ °C	62.5%	MCF-7 and 7402 cells/MCF-7 tumor-bearing mice	199
	MoS_2 nanosheets	Size: ≈50 nm	N.D.	100 μg mL^{-1}	808 nm; 1.0 W cm^{-2} for 5 min	$\Delta T = 14.4$ °C	—	4T1 cells/4T1 tumor-bearing mice	200
	MoO_{3-x} quantum dots	Size: 2.5 nm	600–800 nm	2 mg mL^{-1}	880 nm; 2.0 W cm^{-2} for 10 min	$\Delta T \approx 25.0$ °C	25.5%	HeLa and L02 cells/HeLa-tumor-bearing mice	149
	MoO_{3-x} quantum dots	Size: 5.63 nm	650–800 nm	3 mg mL^{-1}	808 nm, 2.0 W cm^{-2} for 5 min	$\Delta T = 47.7$ °C	40.01%	4T1 cells	201
	Mo_2C quantum dots	6 nm	700–850 nm	100 μg mL^{-1}	808 nm; 0.64 W cm^{-2} for 5 min	$\Delta T = 36.0$ °C	42.9%	B16-10F and A549 cells/B16-10F tumor-bearing mice	202
	MoS_2 nanoflakes functionalized with PEG	Size: 90 nm	N.D.	80 μg mL^{-1}	808 nm; 2.0 W cm^{-2} for 5 min	$\Delta T = 47.0$ °C	27.6%	Hela and 4T1 cells/4T1 tumor-bearing mice	203
	MoS_2 nanoflakes functionalized with PEG	Size: 90 nm	N.D.	200 μg mL^{-1}	808 nm; 1.0 W cm^{-2} for 5 min	$\Delta T = 25.6$ °C	—	4T1 and RAW 264.7 cells/4T1 tumor-bearing mice	204
	MoS_2 nanodots functionalized with GSH	21 nm	N.D.	100 μg mL^{-1}	808 nm, 0.5 W cm^{-2} for 5 min	$\Delta T \approx 27.5$ °C	—	4T1 cells/4T1 tumor-bearing mice	205
	MoS_2 nanodots	Size: 6 nm	N.D.	500 μg mL^{-1}	808 nm; 2.0 W cm^{-2} for 5 min	$\Delta T = 10.0$ °C	—	HepG2 cells	206
	$MoSe_2$ nanodots	Size: 2.32 nm; height: 0.7 to 2.1 nm	N.D.	60 μg mL^{-1}	785 nm; 2.0 W cm^{-2} for 5 min	$\Delta T \approx 35.0$ °C	46.5%	HeLa cells	147
	$MoSe_2$ nanodots assembled with BSA into nanospheres functionalized with FA	Size nanodots: 3.8 nm; total size: 139.8 nm	N.D.	200 μg mL^{-1}	808 nm, 1.0 W cm^{-2} for 5 min	$T_{max} = 41.0$ °C	—	4T1 cells/4T1 tumor-bearing mice	207
	MoO_{3-x} hollow nanospheres functionalized with PEG	Size: 142 nm	700–1000 nm	0.5 mg mL^{-1}	808 nm; 1.0 W cm^{-2} for 10 min	$T_{max} \approx 54.0$ °C	≈22.64%	Hela, MCF-7 and PANC-1 cells/PANC-1 tumor-bearing mice	156

Table 1 *(Contd.)*

Materials	Morphology and surface modification	General properties	Absorption band	Dose	PTT			Type of cancer *in vitro*/*in vivo*	Ref.
					Laser	Temperature	PTT conversion efficiency		
Iron oxide	Fe_3O_4 particles functionalized with PEG or citrate	Size PEG stabilized Fe_3O_4: 300 nm; size citrate stabilized Fe_3O_4: 240 nm	N.D.	50 μg mL^{-1}	808 nm, 6.6 W cm^{-2} for 5 min	ΔT = 52.2 °C (PEG); ΔT = 31.5 °C (Cit)	16.9% (PEG); 15.9% (Cit)	A549 cells/A549 tumor-bearing mice	208
	Fe core/Fe_3O_4 shell nanoparticles functionalized with PEG	Fe core: 9.5 nm; total size: 13.4 nm	N.D.	0.2 mg mL^{-1}	808 nm; 0.38 W cm^{-2} for ≈8 min	ΔT ≈ 17.5 °C	≈20%	Hela cells/HeLa tumour bearing mice	209
	Porous iron oxide nanoparticles	Size: 260 nm	680–980 nm	200 μg Fe mL^{-1}	808 nm; 1 W cm^{-2} for 10 min	ΔT = 31.0 °C	45.99%	4T1 cells	159
	Fe_3O_4 nanoparticles coated with polysiloxane-containing diblock copolymer	Polymer layer: 3–5 nm; total size: 15 nm	N.D.	0.5 mg Fe mL^{-1}	885 nm; 2.5 W cm^{-2} for 10 min	T_{max} = 56.4 °C	—	SUM-159 cells/SUM-159 tumor-bearing mice	210
	Fe_3O_4 nanoparticle modification with carboxymethyl chitosan	Carboxymethyl chitosan thickness: ≈25 nm; total size: 228 nm	800 nm	300 μg mL^{-1}	808 nm; 2.0 W cm^{-2} for 5 min	ΔT = 54.2 °C	—	KB, MCF-7 and S180 cells/S180 tumor-bearing mice	211
	Fe_3O_4 clusters coated with polydopamine	Polydopamine shell: 27 nm; total size: 364 nm	≈400–550 nm	50 μg mL^{-1}	808 nm laser; 6.6 W cm^{-2} for 8 min	T_{max} ≈ 57.0 °C	13.1%	A549 cells/A549 tumor-bearing mice	212
	Fe_3O_4 cluster	Individual Fe_3O_4 NPs: 15 nm; size: 225 nm with a spherical shape	≈400–600 nm	50 μg mL^{-1}	808 nm; 5.0 W cm^{-2} for 3 min	T_{max} = 51.4 °C	—	A549 cells/A549 tumor-bearing mice	213
	Gold nanopopcorns containing a self-assembled Fe_3O_4 cluster core functionalized with PEG	Fe_3O_4 cluster size: 87 nm; external Au structure: ≈30 nm; total size: 158 nm	N.D.	4.0 μg mL^{-1}	808 nm, 0.55 W cm^{-2} for 10 min	ΔT = 40.0 °C	61%	KB-3-1 head and neck cancer cells	214
	Nanocubes	Size: 20 nm	N.D.	0.7 mg mL^{-1}	808 nm; 0.3 and 0.8 W cm^{-2} for 5 min	ΔT = 7.0 °C (0.3 W cm^2); ΔT = 22.0 °C (0.8 W cm^2)	—	SKOV3, PC3 and A431 cells/A431 tumor-bearing mice	215
Copper	Iodine-131-doped CuS nanoparticles functionalized with PEG	Size: ≈20 nm	700–1000 nm	60 μg mL^{-1}	808 nm; 0.8 W cm^{-2} for 5 min	ΔT = 50.0 °C	—	4T1 cells/4T1 tumor-bearing mice	216
	Artesunate-loaded transferrin modified hollow mesoporous CuS nanoparticles	Mesoporous shell: 20 nm; total size: 205 nm	N.D.	200 μg mL^{-1}	808 nm; 2.0 W cm^{-2} for 5 min	ΔT = 54.0 °C	—	MCF-7 cells/MCF-7 tumor-bearing mice	163
	CuS nanoparticles functionalized with DSPE-PEG2000	Size: ≈3.8 nm	700–1100 nm	500 μg mL^{-1}	808 nm; 1.0 W cm^{-2} in 12 min	ΔT = 23.3 °C	≈31.4%	HeLa cells/S180 tumor-bearing mice	217
	$Cu_{2-x}Se$ nanoparticles dimercapto PEG	Size: 3.6 nm	≈600–1100 nm	100 μg mL^{-1}	808 nm; 0.75 W cm^{-2} for 10 min	ΔT = 75.0 °C	64.8%	4T1 cells/4T1 tumor-bearing mice	218
	Plate like Cu_9S_5 nanocrystals	Size: ≈70 nm; thickness: 13 nm	N.D.	40 μg mL^{-1}	980 nm; 0.51 W cm^{-2} for 7 min	ΔT = 15.1 °C	25.7%	HeLa cells/SCID tumor-bearing mice	219

Table 1 *(Contd.)*

Materials	Morphology and surface modification	General properties	Absorption band	Dose	PTT			Type of cancer *in vitro*/*in vivo*	Ref.
					Laser	Temperature	PTT conversion efficiency		
	$Cu_{2-x}S$ nanocrystals	6.5 nm	N.D.	200 μg mL^{-1}	808 nm; 2.3 W cm^{-2} for 10 min	ΔT = 30.6 °C	16.3%	B16 cells/B16 tumor-bearing mice	220
	Cu nanowires functionalized with PEG	Size: ≈46 nm; L: ≈40 μm	N.D.	50 mg mL^{-1}	808 nm; 1.5 W cm^{-2} for 10 min	T_{max} = 65.0 °C	12.5%	CT26 cells/CT26 tumor-bearing mice	221
	Ultrasmall $Cu_{2-x}S$ nanodots	Size: ≈2 nm	800–1200 nm	50 μg mL^{-1}	980 nm; 1.41 W cm^{-2} for 5 min	T_{max} ≈ 37.0 °C	—	HeLa cells/HeLa tumor-bearing mice	222
	CuS nanodots	Size: 4.3 nm	≈990 nm	100 μg mL^{-1}	808 nm; 2.0 W cm^{-2} for 10 min	ΔT = 27.0 °C	—	4T1 cells/4T1 tumors bearing mice	223
	CuS nanoplates	L: 59.4 nm; W: 23.8 nm	800–1100 nm	400 μg mL^{-1}	980 nm; 4.0 W cm^{-2} for 10 min	ΔT ≈ 20.0 °C	—	HeLa, HUVEC, RAW 264.7 and KB cells/ICR mice	224
Carbon	Single-walled carbon nanotubes functionalized with FA	D: 1–2 nm; L: 0.5–100 μm;	≈400–500 nm	1 mg mL^{-1}	800 nm; 1.726 W cm^{-2} for 3 min	ΔT = 64.6 °C	—	MCF7 cells	92
	Multi-walled carbon nanotubes functionalized with PEG	D: 10 nm; L: 50–150 nm	N.D.	2 and 4 mg kg^{-1}	808 nm; 3.5 W cm^{-2} for 1.5 min	T_{max} = 39.0 °C (2 mg kg^{-1}); T_{max} = 44.0 °C (4 mg kg^{-1})	—	A549 cells/A549 tumor-bearing mice	113
	Single-walled carbon nanotubes	D: 0.7–1.3 nm	500–650 nm	0.35 mg mL^{-1}	808 nm; 1.0 W cm^{-2} for 3 min	ΔT = 60.0 °C	—	MDA-MB-435 cells/ MDA-MB-435 tumor-bearing mice	103
	Single-walled carbon nanotube-embedded indocyanine green–HA nanoparticles	Size: 389 nm	N.D.	Indocyanine (10 μg mL^{-1}) or nanotubes (35 μg mL^{-1})	808 nm; 0.3 W cm^{-2} for ≈4 min	ΔT = 30.0 °C	—	SCC-7 and NIH-3T3 cells/ SCC7 tumor-bearing mice	102
	Reduced graphene oxide nanocomposite	Size: ≈300 nm; thick: 3.5 nm	N.D.	120 μg mL^{-1}	808 nm; 1.5 W cm^{-2} for 5 min	ΔT = 30.0 °C	49.1%	MCF-10A and MCF-7 cells/4T1 tumor-bearing mice	96
	Indocyanine green-loaded polydopamine-reduced graphene oxide nanocomposites	Size: 1.0 μm; thick: 2.74 nm	750–850 nm	20 mg L^{-1}	808 nm, 0.6 W cm^{-2} for 5 min	T_{max} = 54.4 °C	—	BEAS-2B and 4T1 cells/4T1 tumor-bearing mice	94
	Gold nanoparticles onto graphene oxide nanocomposite	Graphene oxide D: 230; and thickness: 15 nm; gold nanoparticles size: 15 nm	N.D.	100 mg mL^{-1}	808 nm; 0.3 W cm^{-2} for 10 min	ΔT = 23.0 °C	—	SCC7 cells/SCC7 tumor-bearing mice	117

Table 1 *(Contd.)*

Materials	Morphology and surface modification	General properties	Absorption band	Dose	PTT			Type of cancer *in vitro*/*in vivo*	Ref.
					Laser	Temperature	PTT conversion efficiency		
	Graphene oxide-coated gold superparticles	D: ≈90 nm and ≈130 changing the concentration of gold nanoparticles	N.D.	100 μg mL^{-1}	808 nm; 1.0 W cm^{-2} for 5 min	ΔT = 49.3 °C	—	U87MG cells/ U87MG tumor-bearing mice	116
	Carbon dots	Size: 2.9 ± 0.5 nm	600–900 nm	125 μg mL^{-1}	808 nm; 2.0 W cm^{-2} for 10 min	ΔT = 37.0 °C	38.7%	HepG2 and CT26 cells/CT26 tumor-bearing mice	97
	Carbon dots with chitosan	Size: 65 nm with a quasisphere morphology	235–260 nm	0.05 mg mL^{-1}	808 nm; 1.5 W cm^{-2} for 5 min	ΔT = 20.0 °C	25.2%	4T1 cells/4T1 tumor-bearing mice	93
	Graphene nanodots	Size: ≈5 nm	655 nm	2 mg mL^{-1}	670 nm; 0.3 W cm^{-2} for 30 min	T_{max} ≈ 50.0 °C	—	MDA-MB231 cells/ MDA-MB231 tumor-bearing mice	225

irradiation with the NIR laser (808 nm, 2 W cm^{-2} for 5 min), reaching the maximum temperature of 66.7 °C. Furthermore, a temperature-responsive drug release from the gold shell coated liposomes was observed. In fact, the resveratrol release increased upon irradiation with the NIR laser due to the phase change of the liposomes. In the *in vitro* studies, the photothermal effect mediated by the gold nanoshell coated chitosan modified liposomes (54 μg mL^{-1}) induced a reduction of the HeLa cell viability up to 57.3%. This cytotoxic effect was further enhanced when the heat generated by these nanomaterials was combined with the resveratrol action, leading to cell viability values less than 20%. Similarly, Manivasagan *et al.* developed anti-EGFR paclitaxel loaded-thiol chitosan-layered gold nanoshells for the fluorescence/photoacoustic imaging and chemo-PTT of cancer (Fig. 3).[78] In this approach, gold nanoshells composed of gold spheres with a 9 nm diameter were created on the surface of silica cores (120 nm). Then, the surface of this material was functionalized with thiolated chitosan through gold–thiol interactions and further conjugated with an anti-EGFR antibody. The resulting nanoparticles presented a strong absorption band in the 700–1200 nm region with a peak of absorption at 799 nm. This absorption peak resulted in heat generation upon the irradiation of the chitosan-layered gold nanoshells with a NIR laser (808, 1.2 W cm^{-2} for 5 min), reaching 52.7 °C when a nanoparticle concentration of 175 μg mL^{-1} was used. Additionally, these authors also observed that the heat generated could be used to trigger the paclitaxel release from the chitosan layer present on the surface of the gold nanoshells, in fact after 48 h, at pH 5, the group subjected to 5 irradiation cycles released 91.09% of the drug, in contrasting to 53.83% recorded for the non-irradiated group. The *in vivo* assays demonstrated that the tumor irradiation with a NIR laser (808, 1.2 W cm^{-2} for 5 min) 5 h after the intravenous administration of the anti-EGFR paclitaxel loaded-thiol chitosan-layered gold nanoshells (175 μg mL^{-1}) caused an increase in the tumor temperature, reaching a maximum of 61.9 °C. Furthermore, the authors also observed that the combinatorial action of the paclitaxel and PTT resulted in the eradication of the tumors (97.43% tumor inhibition rate).

2.2.2. Gold nanorods. Gold nanorods have been one of the most explored morphologies to develop gold nanostructures for photothermal applications.[79] The gold nanorods present two absorption bands, a weaker one in the visible region of the spectrum (*i.e.* transverse resonance, surface electron oscillation along the nanorod width) and a more intense band that can be fine-tuned to the NIR region (*i.e.* longitudinal resonance, surface electron oscillation along the nanorod length).[21,80] The absorption band corresponding to the longitudinal resonance is dependent on the nanorod aspect ratio (*i.e.* rod length/width coefficient), and nanorods with aspect ratios between 3 and 6.6 were applicable in PTT.[81] Mackey and colleagues studied the photothermal potential of nanorods with different dimensions (length × width: 38 × 11, 28 × 8, and 17 × 5 nm).[82] The obtained results demonstrated that despite the similar aspect ratios (3.4–3.5), the different gold nanorods

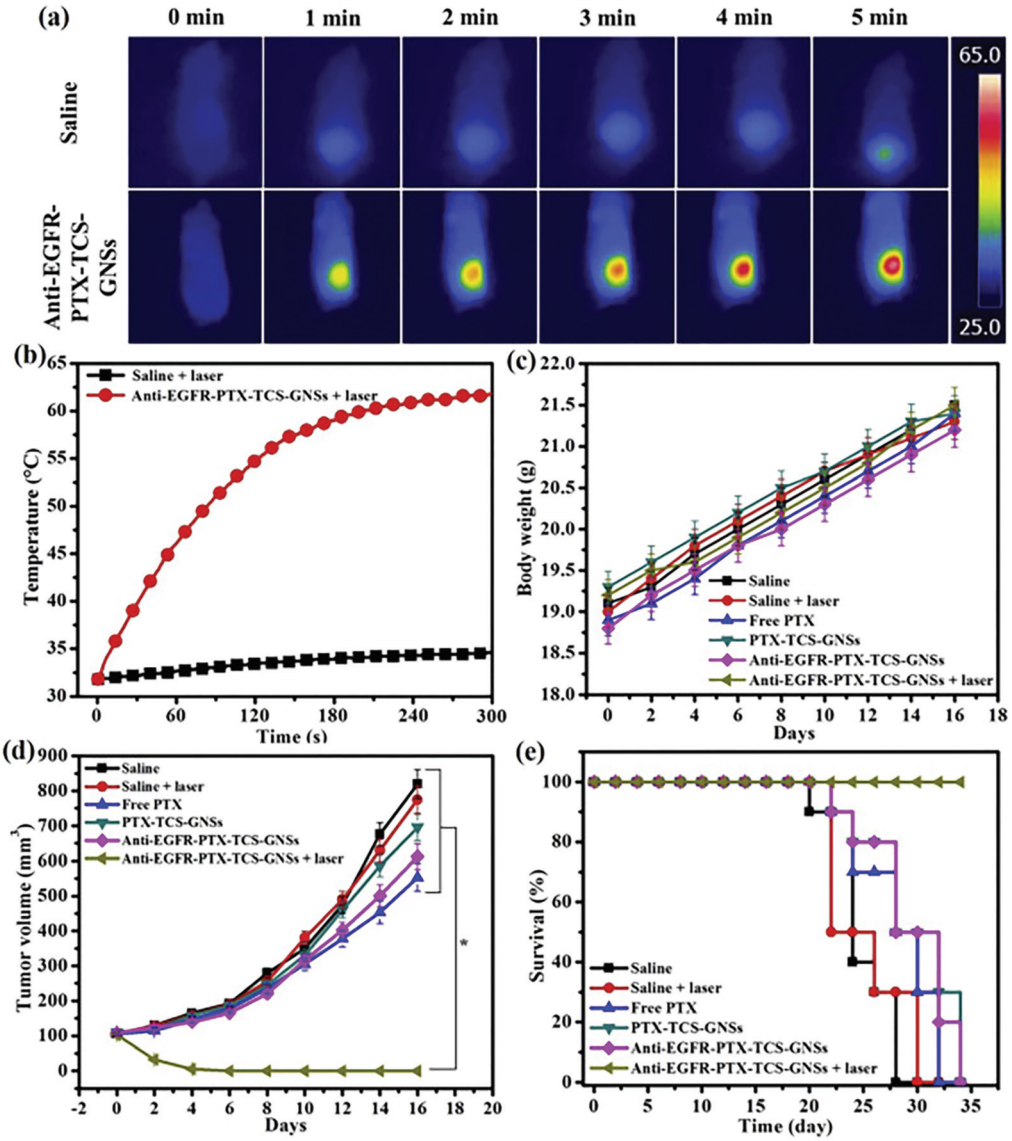

Fig. 3 Evaluation of the antitumoral capacity of anti-EGFR-PTX-TCS gold nanoshells. Thermal images (A) and temperature variation curves (B) of tumors after irradiation with the NIR laser (808 nm, 1.2 W cm^{-2}). Analysis of the mouse body weight changes (C), tumor volume evolution (D) and mouse survival (E) after different treatments. Reprinted from P. Manivasagan, S. W. Jun, G. Hoang, S. Mondal, H. Kim, V. H. M. Doan, J. Kim, C.-S. Kim, J. Oh, Anti-EGFR antibody conjugated thiol chitosan-layered gold nanoshells for dual-modal imaging-guided cancer combination therapy, *J. Controlled Release*, **311–312**, 26–42, Copyright (2019), with permission from Elsevier.

presented longitudinal absorption peaks at 740, 770 and 755 nm for 38 × 11, 28 × 8, and 17 × 5 nm nanorods, respectively. This difference resulted in an increased heat conversion capacity for the 28 × 8 nanorods after irradiation with a NIR laser (808 nm and 5.8 W cm^{-2}) for 2 min, and the photothermal heat conversion factor was 2.05 and 1.40 times higher than that recorded for the 38 × 11 and 17 × 5 nm nanorods. Moreover, the authors also reported an increased cytotoxicity towards HSC-3 cells (oral squamous cell carcinoma) based on the photothermal effect of the 28 × 8 nm gold nanorods, with the cell viability values of ≈100, ≈17, and ≈29% for nanorods with dimensions of 38 × 11, 28 × 8, and 17 × 5 nm. Zhang and coworkers developed PEG-biotin functionalized DNA conjugated gold nanorods for the targeted chemo-PTT of breast cancer.[83] The produced gold nanorods presented an aspect ratio of 3.5 with a length × width of 50 × 14 nm. The authors modified the nanorod surface by using thiolated-PEG modified with biotin and thiolated-DNA enriched with doxorubicin (DOX) for promoting the establishment of gold–thiol interactions. The produced nanomaterials presented the characteristic absorption peaks of gold nanorods at 512 nm (transversal surface plasmonic resonance) and 806 nm (longitudinal surface plasmonic resonance), which could be exploited to mediate a strong photothermal effect reaching ≈45 °C after irradiation with a NIR laser (808 nm, 5 W cm^{-2} for 30 min, gold nanorods at 5.82 μg mL^{-1}). On the other hand, the gold

nanorods presented a pH and NIR responsive drug release due to the DOX intercalation with the DNA grafted on the particle surface; ≈60% drug was released when irradiated with a NIR laser (808 nm, 5 W cm^{-2} for 30 min) and ≈50% after being incubated at pH 5.0. In the *in vitro* assays, the authors observed that the combinatorial treatment mediated by the gold nanorods (gold nanorods at 5.82 μg mL^{-1} and DOX 2 μM, NIR laser 808 nm, 5 W cm^{-2} for 30 min) inhibited the MCF-7/ADR cell growth in 81% of the cases.

2.2.3. Gold nanostars. The gold nanostar absorption band is dependent on the core size and tip length, width, and number.[84] In general, an increase in the gold nanostar core size, tip length and sharper tips promotes a shift in the absorption peak to the NIR region.[85] Espinosa *et al.* produced gold nanostars with 25, 55, 85, 120, and 150 nm diameters and observed that the samples with 25 nm diameters presented two absorption peaks at 550 and 700 nm, whereas the samples with 55, 85, 120, and 150 nm diameters presented a single absorption band at 790, 800, 900, and 950 nm, respectively.[86] Furthermore, the authors also reported that upon irradiation with the NIR laser (808 nm, 1 W cm^{-2}) for 10 min, the nanostars with diameters of 25, 85, and 150 nm mediated an increase in temperature of ≈18 °C, ≈45 °C, and ≈36 °C. Xia and colleagues developed IR-780 iodine-loaded gold nanostars functionalized with matrix metalloproteinases (MMP2), polypeptides (Ac-GPLGIAGQ) and bovine serum albumin (BSA) for lung cancer imaging and photothermal/photodynamic therapy.[87] For that purpose, the gold nanostars were conjugated with BSA *via* gold thiol interactions. Then, MMP2 polypeptides were grafted on the nanostar surface through carbodiimide chemistry and loaded with the IR-780 molecules. The resulting nanoparticles presented a mean diameter of 80 nm and a strong absorption band in the 700–800 nm region. The data obtained revealed that the irradiation of the gold nanostars (20 μg mL^{-1}) with a NIR laser (808 nm, 0.8 W cm^{-2} for 5 min) could mediate a temperature increase up to 63 °C. In the *in vivo* studies, the intravenous administration of the IR-780 iodine-loaded gold nanostar functionalized MMP2 and BSA (IR-780, 1 mg kg^{-1}) mediated an increase in the tumor temperature up to 46 °C (808 nm, 0.8 W cm^{-2} for 5 min), which combined with IR-780 action led to a 93% reduction of the tumor volume.

2.2.4. Gold nanocages. Gold nanocages, nanostructures where gold is only present at the particle surface, present an absorbance band that can be tuned to the NIR region by optimizing the wall thickness.[88] In fact, the increase in the amount of the gold source during the synthesis procedure is linked to a red-shift in the absorption peak.[89] Huang and coworkers developed polyethyleneimine (PEI)-modified and folate receptor-targeted PEGylated gold nanocages enriched with a microRNA-181b inhibitor aimed for the cancer gene and PTT.[90] The gold cages had a 50 nm size, a hollow structure, and pores with 5 nm. Then, thiol-PEG-folic acid (FA) chains were attached on the particle surface *via* gold–thiol interactions and the PEI was conjugated using lipoic acid as a linker. The resulting nanoparticles presented an absorption peak at 802 nm and upon irradiation with a NIR laser (808 nm, 1.25 W cm^{-2} for 10 min) induced a temperature increase up to ≈55 °C, when a concentration of 9.7 μg mL^{-1} was used. In the *in vivo* studies, the intravenous administration of gold nanocages (gold content at 8.5 mg kg^{-1}) resulted in an increase in the temperature up to 53.6 °C, which combined with the action of the anti-microRNA-181b inhibited the liver tumor progression and increased the mouse median survival times from 36 to 60 days. In turn, Sun and colleagues developed DOX-loaded gold nanocages coated with 4T1 cancer cell membranes for the chemo/PTT of breast cancer.[91] For that purpose, DOX-loaded gold nanoshells with 70.5 nm diameter were extruded with 4T1 cell membrane vesicles through a 100 nm polycarbonate membrane. The resulting nanomaterials presented an absorption peak at 760 nm and could mediate a temperature increase of ≈25 °C upon irradiation with a NIR laser (808 nm, 2.5 W cm^{-2} for 8 min). Moreover, in the *in vivo* studies the combinatorial treatment (intravenous administration of 91 mg kg^{-1} of gold nanoshells) suppressed the tumor progression and decreased the number of lung metastases by 98.5%.

2.3. Carbon-based nanomaterials

Carbon-based materials, principally carbon nanotubes and graphene, have been widely explored for cancer photothermal applications.[92–94] The graphitic structure of carbon-based materials endows them with a strong optical absorption in the NIR region of the spectra and high photothermal conversion efficiencies.[95–97] In these materials, after the light interaction, the energy is transferred to the lattice by electron–phonon coupling generating heat.[95] Furthermore, the intrinsic properties of the sp^3 and sp^2 lattices of the carbon-based materials also endow them with high thermal conductivity.[98,99]

2.3.1. Carbon nanotubes. Carbon nanotubes were initially described by Iijima in 1991[100] and are the most explored carbon-based nanomaterials in the literature for biomedical applications.[52,101–104] These materials are usually synthesized using methodologies based on arc discharge or chemical vapor deposition of graphite.[105] The carbon nanotubes are cylindrical tubes of sp^2 graphite sheets with diameters within the nanoscale, which can be organized in single-walled or multi-walled carbon nanotubes.[106,107] Moreover, the electronic and optical properties of these nanomaterials depend on the diameter and the relative orientation of the graphene basic hexagons with respect to the axis tube, and the latter is usually identified by the so called "chiral vector" – two integers (n,m).[52,108,109] The synthesis procedures for single-walled carbon nanotubes usually result in a mixture of nanostructures with different chiral vectors.[110] Therefore, the absorption spectra of these samples comprise several absorption peaks superimposed, according to the different chiralities of carbon nanotubes.[111] On the other hand, the multi-walled carbon nanotubes present a simpler absorption spectrum, in which the absorbance monotonically decreases with the wavelength increase.[112,113] This characteristic of the multi-walled

carbon nanotubes prompted their application in cancer PTT. Marangon and colleagues developed *m*-tetrahydroxyphenylchlorin loaded multi-walled carbon nanotubes for the photodynamic therapy and PTT of ovarian cancer.[114] The produced multi-walled carbon nanotubes presented a mean diameter of 39 nm and a length of 400 nm as well as the typical absorption spectra (*i.e.* constant decrease in the absorbance when progressing to the NIR region of the spectra). Furthermore, the authors observed that the multi-walled carbon nanotubes at 20 μg mL^{-1} could mediate an increase in the temperature of 10 °C upon 80 seconds of NIR laser irradiation (808 nm and 2 W cm^{-2}), whereas at a concentration of 100 μg mL^{-1} a temperature increase of 50 °C could be achieved after 60 seconds of irradiation. Additionally, the authors observed that the multi-walled carbon nanotubes could induce the photothermal ablation of SKOV3 cancer cells, and only 10% of SKOV3 cells remained viable after NIR laser irradiation (808 nm, 2.3 W cm^{-2}, 200 seconds, and 20 μg mL^{-1}). The cytotoxic effect of nanotubes was further improved by combining them with the *m*-tetrahydroxyphenylchlorin action. Similarly, Wang *et al.* produced DOX loaded multi-walled carbon nanotubes functionalized with poly(*N*-vinyl pyrrole), PEG and Fa for the combined chemo-PTT of cancer.[115] The authors reported that the carbon nanotubes presented 8 to 15 nm diameter and less than 1 μm length. These materials were modified by promoting the oxidative polymerization of *N*-vinyl pyrrole on their surface, followed by the addition of Fa-terminated PEG (FA-PEG-SH) through thiol–ene click chemistry. The resulting nanostructures were able to induce an increase in the temperature up to ≈45 °C at a concentration of 50 μg mL^{-1}, after NIR laser irradiation (808 nm, 1.5 W cm^{-2} for 6 min). This capacity was maintained even after five on/off cycles. In the *in vitro* studies, the authors demonstrated that the administration of the functionalized multi-walled carbon nanotubes at 50 μg mL^{-1} induced the reduction of the HeLa cell viability to ≈40% after NIR laser irradiation (808 nm, 1.5 W cm^{-2} for 6 min). Moreover, an increased cytotoxic effect was observed with the combined action of DOX and multi-walled carbon nanotube photothermal effect, and only ≈20% of cells remained viable.

Zhang and coworkers developed PEGylated multi-walled carbon nanotubes modified with CREKA for the targeted PTT.[113] The nanomaterials presented 10 nm diameter and 50 to 150 nm length and the characteristic multi-walled carbon nanotube absorption spectra. Furthermore, the authors observed that 24 hours after the intravenous administration of these targeted carbon nanotubes at a dose of 4 mg kg^{-1} in A549 tumor xenograft-bearing mouse models, the NIR laser irradiation (808 nm, 3.5 W cm^{-2} for 1 min) induced an increase in the temperature up to 55.17 °C within the tumor microenvironment. Furthermore, the single intravenous administration followed by four irradiation cycles resulted in the almost complete eradication of the tumor xenografts, without eliciting noticeable side-effects (Fig. 4).

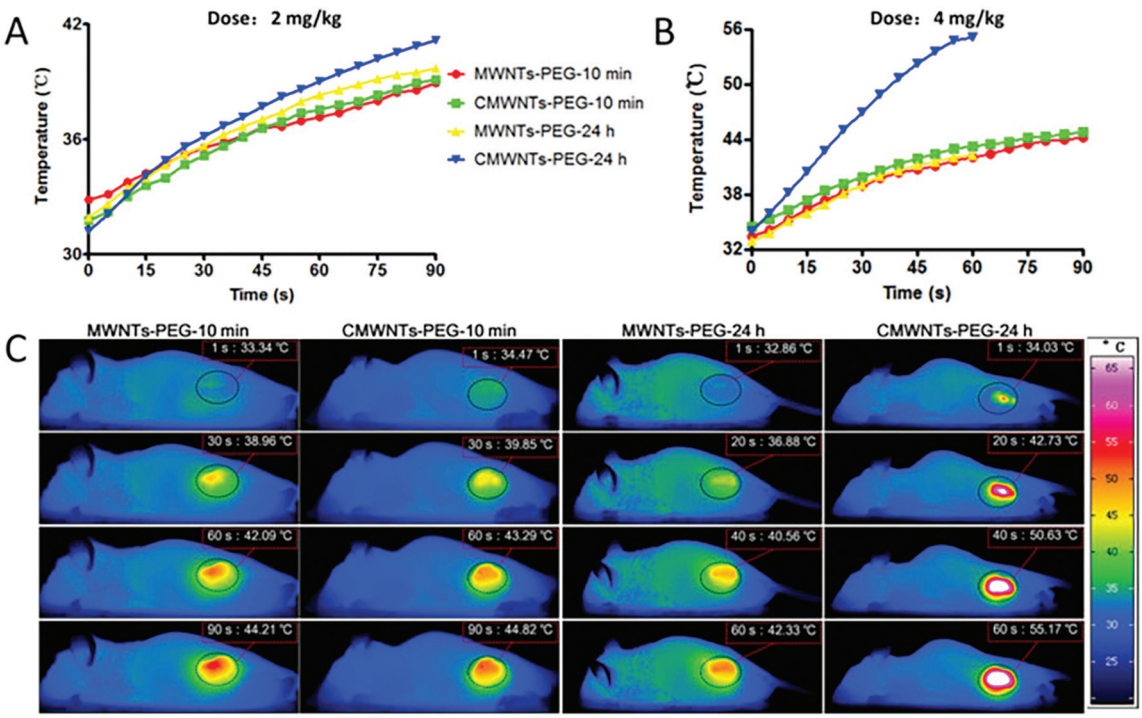

Fig. 4 Evaluation of the multi-walled carbon nanotube (CMWNTs-PEG) photothermal effect. Temperature variation curves of tumors after injection doses of 2 mg kg^{-1} (A) and 4 mg kg^{-1} (B) and NIR laser irradiation (808 nm, 3.5 W cm^{-2}). Thermal images of tumor-bearing mice treated with a MWNT dose of 4 mg kg^{-1}. (C) Reprinted from B. Zhang, H. Wang, S. Shen, X. She, W. Shi, J. Chen, Q. Zhang, Y. Hu, Z. Pang, X. Jiang, Fibrin-targeting peptide CREKA-conjugated multi-walled carbon nanotubes for self-amplified photothermal therapy of tumor, *Biomaterials*, **79**, 46–55, Copyright (2016), with permission from Elsevier.

2.3.2. Graphene-based materials. Recently, graphene-based materials captured the attention of researchers for being applied in cancer PTT.[116–118] Graphene is the building block of other graphite materials, such as 3D graphite, carbon nanotubes and fullerenes.[119] This material presents a honeycomb lattice formed by a single-atom-thick layer of sp^2 hybridized carbon atoms and can be classified according to the oxygen content, the number of layers in the sheet, or their chemical composition.[120] Among the most common graphene materials, the graphene oxide and reduced graphene oxide have been one of the most explored for biomedical applications.[121] These graphene derivatives are characterized by presenting various oxygen-based groups such as epoxide, carbonyl, carboxyl, and hydroxyl groups.[122] Nevertheless, the reduced graphene oxide presents an enhanced absorbance in the NIR region of the spectrum, which makes it a better candidate for photothermal applications.[123] Lima-Sousa and colleagues functionalized the reduced graphene oxide with hyaluronic acid (HA) for mediating the targeted PTT of cancer.[124] These authors promoted the reduction of graphene oxide using ascorbic acid and the surface functionalization was achieved through hydrophobic interactions between the carbon lattice and a HA-based amphiphilic polymer (HA grafted onto poly(maleic anhydride-*alt*-1-octadecene)). The obtained nanomaterial presented a mean size of 108 nm and an absorbance in the NIR region superior to that of graphene oxide. Furthermore, the authors also reported that the functionalized reduced graphene oxide (75 μg mL^{-1}) induced an increase in the temperature up to 33 °C after NIR laser irradiation (808 nm, 1.7 W cm^{-2} for 5 min). Moreover, in the *in vitro* studies the heat generated upon the irradiation of the reduced graphene oxide-based nanomaterials induced the reduction of the MCF-7 cancer cell viability to ≈6%.

Cheon *et al.* developed reduced graphene oxide modified with serum albumin and loaded with DOX for the chemo-PTT of brain tumors.[125] The authors conjugated the serum albumin with the graphene oxide by promoting the simultaneous reduction of these nanomaterials, and subsequently performing the encapsulation of DOX on the surface of graphene oxide sheets. The obtained nanomaterials presented an enhanced absorption in the NIR region of the spectra, when compared to the non-reduced graphene oxide, and upon NIR laser irradiation (808 nm, 5.5 W cm^{-2} for 3 min) the serum albumin coated reduced graphene oxide (30 μg mL^{-1}) induced a temperature increase up to ≈60 °C. Moreover, these authors also demonstrated that this increase in the temperature could be exploited to trigger the drug release and induce the death of U87MG cancer cells, with 21.8% and 1.76% of viable cells for the groups treated with only photothermal or chemo-PTT, respectively.

Roy and coworkers modified reduced graphene oxide nanosheets with poly(allylamine hydrochloride) for mediating the chemo-PTT of breast cancer.[126] The functionalized reduced graphene oxide presented an average size of 115 nm and a broad absorption throughout the visible and NIR regions of the spectra. Moreover, the authors also demonstrated that the irradiation of the functionalized reduced graphene oxide (150 μg mL^{-1}) with a NIR laser (808 nm, 6 W cm^{-2} for 6 min) could induce a temperature increase to values greater than 45 °C. Furthermore, in the *in vitro* studies, a combinatorial therapeutic modality mediated by the DOX delivery and photothermal effect resulted in an enhanced cytotoxicity towards MCF-7 cells, with 70% and 6% of viable cells in the groups treated by photothermal or chemo-PTT (nanomaterial dose: 5 μg mL^{-1}), respectively.

2.4. Tungsten nanomaterials

Tungsten-based nanomaterials for PTT can be produced by using methodologies such as solution-phase synthesis,[127] vapor-phase synthesis,[128] precipitation routes[129] and hydrothermal methods.[130] Among them, the hydrothermal pathway has been associated with a higher control over the morphology of the particles.[131] Furthermore, the tungsten nanomaterials due to their outer-d valence electrons present a localized SPR, similar to the nanoparticles of noble metals, which can be exploited for enabling a photothermal effect.[132] The localized SPR will be dependent on the doping or stoichiometry of the tungsten nanomaterials and on the optimization of the size and shape of the nanoparticles.[133,134] Among the different doped tungsten nanocrystals, tungsten oxide nanomaterials have been one of the most explored in the literature for biomedical applications.[135–137] This transition metal oxide exhibits a wide band gap of 2.62 eV and a localized SPR.[132,138] Particularly, nonstoichiometric WO_x compositions, such as $W_{20}O_{58}$, $W_{18}O_{49}$ and $W_{24}O_{68}$ (obtained mainly by reduction processes), present a strong NIR absorption, which makes them strong candidates for photothermal applications.[139] Tian and coworkers developed $W_{18}O_{49}$ nanorod coated lentinan for the PTT of breast cancer.[140] The tungsten nanomedicines were produced using a one-pot solvothermal approach mixing tungsten chloride and lentinan. The resulting $W_{18}O_{49}$ nanorods presented a length and width of 180 and 40 nm, respectively, as well as an increased absorbance in the 600 to 1200 nm region. These authors demonstrated that the irradiation (980 nm, 1 W cm^{-2} for 10 min) of the lentinan coated $W_{18}O_{49}$ nanorods (500 μg mL^{-1}) resulted in a temperature increase to ≈55 °C, which could be maintained after 5 on/off irradiation cycles. In the *in vitro* studies, the photothermal effect mediated by the lentinan coated $W_{18}O_{49}$ nanorods (200 μg mL^{-1}) led to the reduction of the MDA-MB-231 cellular viability to 24%. Similarly, Zhou and colleagues produced PEGylated nonstoichiometric $WO_{2.9}$ nanorods for the PTT and imaging of tumors.[141] For that purpose, $WO_{2.9}$ nanorods were produced with a length of 13.1 nm and a width of 4.4 nm *via* a high-temperature pyrolysis method. Subsequently, nanorod PEGylation was performed by exploring the coordination interactions between PEG carboxylate groups and the tungsten oxide surface. Furthermore, the PEGylated $WO_{2.9}$ nanorods present a strong absorption in the NIR region and upon irradiation (980 nm, 0.25 W cm^{-2} for 10 min) a temperature increase of 20.1 °C could be achieved at a dose of 100 μg

mL^{-1}. In the *in vitro* assays, the $WO_{2.9}$ nanomaterials remained biocompatible at concentrations up to 500 μg mL^{-1}, whereas the NIR laser irradiation (980 nm, 0.35 W cm^{-2} for 8 min) induced a reduction in the HeLa cell viability to values less than 20%, even at a dose of 50 μg mL^{-1}. Moreover, the intra-tumoral administration of PEGylated $WO_{2.9}$ nanorods (200 μL at 20 mg kg^{-1}) resulted in a temperature increase (≈20 °C) and a consequent growth inhibition of HeLa tumors after NIR laser irradiation (980 nm, 0.35 W cm^{-2} for 10 min). Sharker *et al.* created dopamine-conjugated HA tungsten oxide nanoparticles for the targeted PTT of breast cancer.[48] In this approach, the HA was conjugated with dopamine *via* carbodiimide chemistry and then assembled on the tungsten oxide nanoparticles at a mild alkaline pH. The resulting nanomaterials presented a mean diameter of 176.25 nm and an absorption peak in the 800 to 1100 nm region. The heat generated by the tungsten oxide nanoparticles (1 mg mL^{-1}) irradiated with a NIR laser (808 nm laser, 2 W cm^{-2} for 5 min) led to a temperature increase up to 44 °C and the reduction of the MDA-MB-231 and A549 cellular viability to 3%. Moreover, the intravenous administration of the dopamine-conjugated HA tungsten oxide nanoparticles (30 mg kg^{-1}) to MDA-MB-231 tumor-bearing mice resulted in the increase of the tumor temperature up to 50 °C after NIR laser irradiation and the reduction of the tumor volume from 400 to 275 mm^3 in 10 days post-injection (Fig. 5).

2.5. Molybdenum nanostructures

Molybdenum-based nanoparticles similar to other transition metal semiconductor nanostructures (*e.g.* tungsten, copper, or iron-based materials) present interesting properties that allow their use in photothermal applications.[142] In fact, these nanomaterials possess a high photothermal conversion efficiency and a SPR that can be fine-tuned to display strong absorption in the NIR region of the spectra.[143] In the literature, it is reported that the doping or stoichiometry of the nanomaterials will affect the physicochemical properties of the molybdenum nanomaterials.[144] In this field, the molybdenum disulfide (MoS_2) and oxygen-deficient molybdenum oxide (MoO_{3-x}) are the most explored for mediating an anticancer photothermal effect.[145,146]

2.5.1. Molybdenum disulfide materials. The MoS_2 structure and electrical properties are analogous to graphene and these nanostructures can be obtained by exfoliation or synthesized with various morphologies such as nanosheets, quantum dots, and nanodots.[147–150] The MoS_2 crystals are composed of S–Mo–S layers, in which the unit cell presents a honeycomb structure containing each Mo atom enclosed by six S atoms.[151] Liu and colleagues modified MoS_2 nanosheets with FA conjugated PEG aiming to use them in the chemo-PTT of breast cancer.[152] In this study, the MoS_2 nanosheets were obtained by chemical exfoliation processes and then functionalized with the heterobifunctional lipoic acid-PEG-Fa by

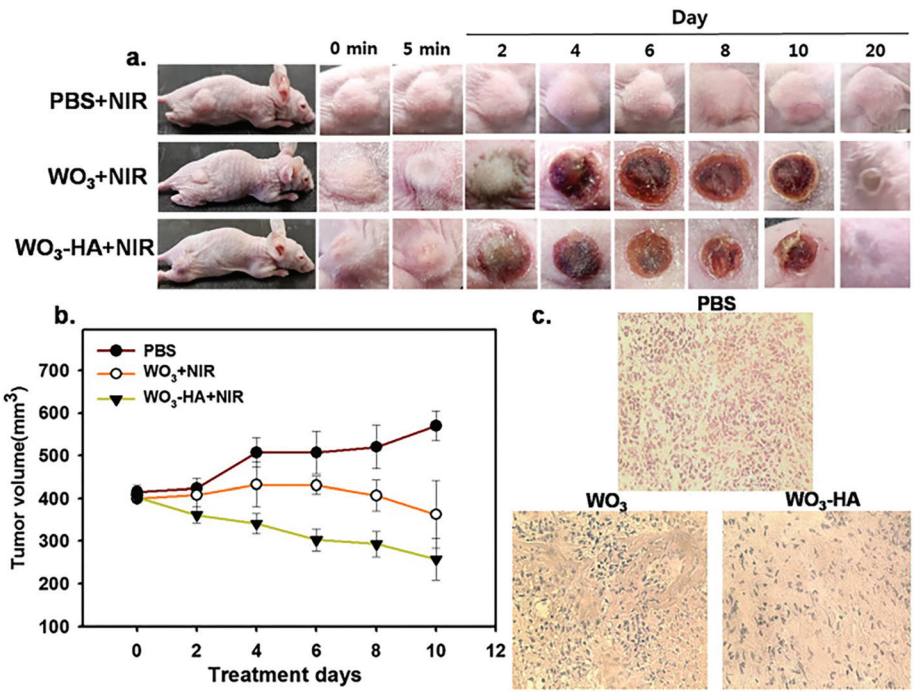

Fig. 5 Evaluation of the photothermal capacity of WO_3-HA nanoparticles. Digital photographs of tumor-bearing mice after treatment with phosphate buffered saline (PBS), free WO_3, and WO_3–HA nanoparticles under 5 min of NIR laser irradiation (808 nm, 2 W cm^{-2}) for 20 days (A). Analysis of the mouse tumor volume during 10 days of treatment (B). Histological images of the tumor tissue with hematoxylin & eosin (H & E) staining after 10 days of treatment (C). Reprinted from S. M. Sharker, S. M. Kim, J. E. Lee, K. H. Choi, G. Shin, S. Lee, K. D. Lee, J. H. Jeong, H. Lee, S. Y. Park, Functionalized biocompatible WO_3 nanoparticles for triggered and targeted *in vitro* and *in vivo* photothermal therapy, *J. Controlled Release*, **217**, 211–220, Copyright (2015), with permission from Elsevier.

exploring hydrophobic interactions. Additionally, the loading of DOX was also achieved by exploring the establishment of π–π stacking and hydrophobic interactions between the drug and the MoS_2 nanosheet lattice. The resulting nanomaterials presented a mean diameter of 50 nm and a thickness of 2 nm. Furthermore, the authors also reported that the PEGylated MoS_2 nanosheets possess a strong NIR absorbance and can mediate a temperature increase up to 60 °C upon NIR laser irradiation (30 μg mL^{-1}, 808, 1 W cm^{-2} for 5 min). On the other hand, the *in vivo* assays revealed that the intra-tumoral administration of DOX-loaded PEGylated MoS_2 nanosheets (20 μL at a dose of 0.34 mg kg^{-1}) followed by irradiation with a NIR laser (808 nm, 0.35 W cm^{-2} for 20 min) caused a temperature increase up to 45 °C and inhibited the growth of 4T1 tumors.

Wang *et al.* produced MoS_2 nanosheets functionalized with a hyperbranched polyglycidyl group and loaded with DOX for the combinatorial therapy of melanoma.[153] For that purpose, MoS_2 nanosheets were prepared through a hydrothermal method and then the hyperbranched polyglycidyl group was physically adsorbed on their surface. The authors reported that the functionalized MoS_2 nanosheets presented a mean diameter of 90 nm (thickness of 3 nm) and an increased absorbance in the NIR region of the spectra, when compared with bare MoS_2 nanosheets. Additionally, the irradiation with a NIR laser (180 μg mL^{-1}, 808 nm, 2 W cm^{-2} for 10 min) induced an increase in the temperature of 34 °C, which mediated the decrease of the B16 cell viability to less than 30%. The authors also demonstrated that the intra-tumoral administration of functionalized MoS_2 nanosheets (40 μL at 2 mg kg^{-1}) followed by irradiation with a NIR laser (808 nm, 1 W cm^{-2} for 10 min) decrease the tumor growth, which was more efficient when combined with the simultaneous action of DOX.

2.5.2. Molybdenum oxide materials. Molybdenum oxides can be found in various stoichiometries from full MoO_3 to more oxygen deficient molybdenum oxide (MoO_{3-x}) or even semi-metallic MoO_2.[154] Liu and colleagues produced MoO_2 nanoparticles with a bow-tie morphology, through a hydrothermal reaction, for mediating the cancer PTT.[155] The resulting nanomaterials presented a strong absorption from the visible to NIR region of the spectra and could mediate a temperature increase up to 63.2 °C upon irradiation with a NIR laser (100 μg mL^{-1}, 980 nm, 2 W cm^{-2} for 3 min). Additionally, the *in vivo* assays demonstrated that the administration of MoO_2 nanoparticles (50 μL at 1 mg kg^{-1}) in mice bearing cervical tumors could cause the increase of the tumor temperature up to 66.3 °C, thus mediating a decrease in the tumor volume from ≈165 to ≈65 mm^3. Bao and coworkers functionalized MoO_{3-x} hollow nanospheres with PEG for the chemo-PTT of pancreatic cancer.[156] The MoO_{3-x} hollow nanospheres were produced though the hydrothermal process, mixing [$(NH_4)_6Mo_7O_{24}\cdot 4H_2O$] and PEG, and then these nanospheres were loaded with campothecin. The resulting nanomaterials presented an average size of 90 nm and a cluster-like structure composed of ultra-small dots with 6 nm diameter. Additionally, the authors reported a strong absorption band in the 700 to 1000 nm region of the spectra and upon NIR laser irradiation (808, 1 W cm^{-2} for 10 min), the PEGylated MoO_{3-x} hollow nanospheres (200 μg mL^{-1}) mediated a temperature increase of ≈20 °C. Moreover, in the *in vivo* assays, the authors observed that the intravenous administration of PEGylated MoO_{3-x} (200 μL at 1 mg kg^{-1}) followed by irradiation with a NIR laser (808 nm, 1 W cm^{-2} for 10 min) increased the tumor temperature up to 48 °C, which combined with the action of the campothecin induced an almost complete tumor eradication with no recurrence at day 15 (Fig. 6).

2.6. Iron-based nanomaterials

Iron oxide nanomaterials have been widely explored to generate hyperthermia effects in the presence of magnetic fields and more recently in response to NIR radiation.[157] Despite the iron nanomaterials (*e.g.* iron oxide) can exhibiting plasmonic properties, they require high energy to induce the excitation of free electrons due to the higher free electron density, when compared to gold nanomaterials. The iron oxide nanoparticles can present different chemical compositions, such as magnetite (Fe_3O_4), maghemite (Fe_2O_3), or non-stoichiometric combinations of the two.[20] These nanomaterials can be synthesized through different methodologies such as co-precipitation, thermal decomposition, and hydrothermal and solvothermal synthesis.[158] Hu and colleagues developed porous hollow Fe_3O_4 nanoparticles modified with polyacrylamide for the combined chemo-PTT of cancer.[159] These nanostructures were produced through a hydrothermal process in a one-pot synthesis including the polyacrylamide. The resulting nanoparticles presented a spherical shape with a diameter of 260 nm and pores of 10 nm size. Moreover, the authors observed a broad absorption peak from the UV to the NIR region of the spectra and upon irradiation with NIR light (808 nm, 1 W cm^{-2} for 10 min) the porous hollow Fe_3O_4 nanoparticles (200 μg mL^{-1}) could mediate a temperature increase of 31 °C. Additionally, the authors also reported that the photothermal effect mediated by the hollow Fe_3O_4 nanoparticles caused a reduction in the 4T1 cellular viability to values lower than 20% (Fig. 7). In turn, Yang and coworkers produced superparamagnetic iron oxide nanoparticles coated with HA for the targeted PTT of breast cancer.[160] The superparamagnetic iron oxide nanoparticles were prepared by a co-precipitation method in alkaline media, followed by modification with 3-aminopropyltrimethoxysilane, and then conjugated with HA *via* carbodiimide chemistry. The nanoparticles presented a mean diameter of 17 nm and upon irradiation with a NIR laser (200 μg mL^{-1}, 808 nm, 1 W cm^{-2} for 9 min) they mediated a temperature increase of ≈18 °C. Moreover, in the *in vitro* studies the heat generated by the superparamagnetic iron oxide nanoparticles caused a ≈70% decrease of the MDA-MB-231 cellular viability. Furthermore, the authors also observed that the intravenous administration and irradiation (20 mg kg^{-1}, 808 nm, 2 W cm^{-2} for 10 min every 24 hours for 8 days) of mice bearing MDA-MB-231 tumors stalled the tumor development with no significant growth being observed for 12 days.

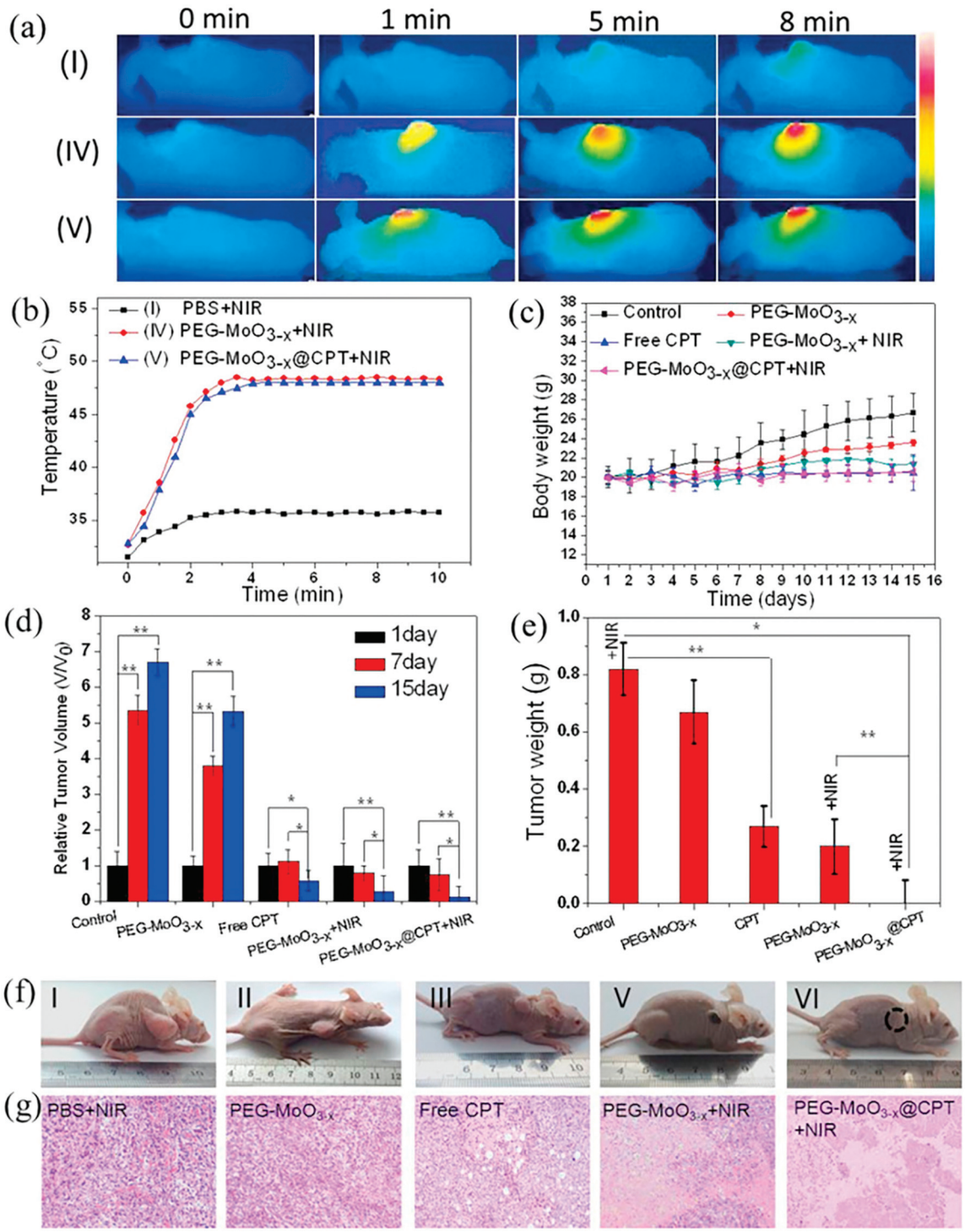

Fig. 6 Evaluation of the MoO_{3-x}-campothecin nanosphere antitumoral capacity. Thermal images (A) and temperature variation curves (B) of tumors after treatment with MoO_{3-x} nanosphere formulations and irradiation with the NIR laser (808 nm, 10 min, 1 W cm^{-2}). Analysis of the mice's body weight (C), tumor volume (D) and tumor weight (E) during the 15 days of treatment. Photographs of mice (F) and tumor H&E stained histological images (G) after 15 days of treatment with MoO_{3-x}-campothecin nanoformulations. Reprinted from S. M. ST. Bao, W. Yin, X. Zheng, X. Zhang, J. Yu, X. Dong, Y. Yong, F. Gao, L. Yan, Z. Gu, One-pot synthesis of PEGylated plasmonic MoO_{3-x} hollow nanospheres for photoacoustic imaging-guided chemo-photothermal combinational therapy of cancer, *Biomaterials*, **76**, 11–24, Copyright (2016), with permission from Elsevier.

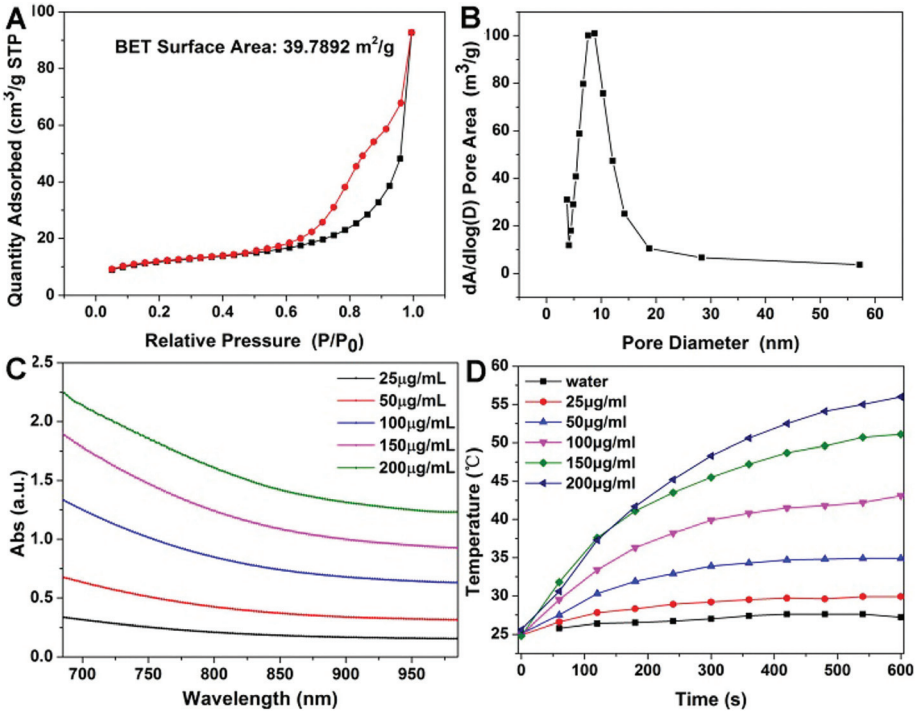

Fig. 7 Physicochemical characterization of porous hollow Fe_3O_4 nanoparticles. (A) Evaluation of the porous hollow Fe_3O_4 nanoparticle porosity (A) and pore size distribution (B) through N_2 adsorption-desorption. UV-Vis absorption spectra of nanoparticles with different concentrations of Fe_3O_4 nanoparticles (C). Temperature variation curves of porous hollow Fe_3O_4 nanoparticles at different concentrations under NIR laser irradiation (808 nm, 1 W cm^{-2}) for 10 min (D). Reprinted from L. Y. Hu, H. Hu, J. Yan, C. Zhang, Y. Li, M. Wang, W. Tan, J. Liu, Y. Pan, Multifunctional Porous Iron Oxide Nanoagents for MRI and Photothermal/Chemo Synergistic Therapy, *Bioconjugate Chem.*, **29**, 1283–1290, Copyright (2018), with permission from ACS Publications.

2.7. Copper nanomaterials

Copper is a transition metal and its nanomaterials can be engineered to be applied in cancer therapy.[161] The synthesis of copper nanoparticles is usually performed through a wet chemical synthesis involving the reduction of copper salts (such as $CuSO_4$, copper(II) acetylacetonate, *etc.*).[161,162] Among the different copper nanomaterials (copper selenide, copper telluride, and copper oxide), copper sulfide has been the most explored for the photothermal treatment of cancer. Copper sulfide and its copper-deficient structures ($Cu_{2-x}S$) present a NIR absorption compared to gold nanostructures, due to the d–d energy band transition of Cu^{2+} ions, which makes them promising photothermal materials. Hou *et al.* developed iron-dependent artesunate loaded hollow porous copper sulfide nanoparticles modified with transferrin for the chemo-PTT of cancer.[163] The resulting nanostructures presented a mean diameter of 205 nm and an increased absorption in the 700 to 1000 nm region of the spectra. Additionally, the authors demonstrated that the NIR laser irradiation (808 nm, 2 W cm^{-2} for 5 min) of the hollow porous copper sulfide nanoparticles (100 μg mL^{-1}) can induce a temperature increase of ≈40 °C, which combined with the iron-dependent artesunate action caused the death of 92.6% of the MCF-7 cancer cells. Moreover, the *in vivo* studies also demonstrated that the combinatorial therapy mediated by the intraperitoneal injection of the hollow porous copper sulfide nanoparticles (100 mg kg^{-1}, 808 nm, 2 W cm^{-2} for 30 s) resulted in a tumor inhibition rate of 74.8% (Fig. 8). Wang and colleagues produced DOX loaded hollow copper sulfide nanoparticles enclosed in a hybrid coating formed by the fusion of the membranes of red blood cells and B16-F10 cells for the combinatorial therapy of melanoma.[164] The nanoparticles presented an average size of 200 nm and a strong absorption at 1064 nm. Furthermore, upon NIR irradiation (1064 nm, 1 W cm^{-2} for 10 min), the hollow copper sulfide nanoparticles mediated a temperature increase up to 75.4 °C. This photothermal capacity remained constant even after four on/off cycles of irradiation. The authors also reported that the combined action of the DOX and the photothermal effect (1064 nm, 1 W cm^{-2} for 10 min) mediated by the fusion membrane coated DOX loaded hollow copper sulfide nanoparticles caused the eradication of melanoma tumors in mice, after an intravenous administration of the nanoparticles at a concentration of 5 mg kg^{-1}.

3. Clinical trials

Currently, there are a wide number of nanomedicines that have been approved for cancer treatment.[165] Nevertheless, despite the promising properties and therapeutic potential

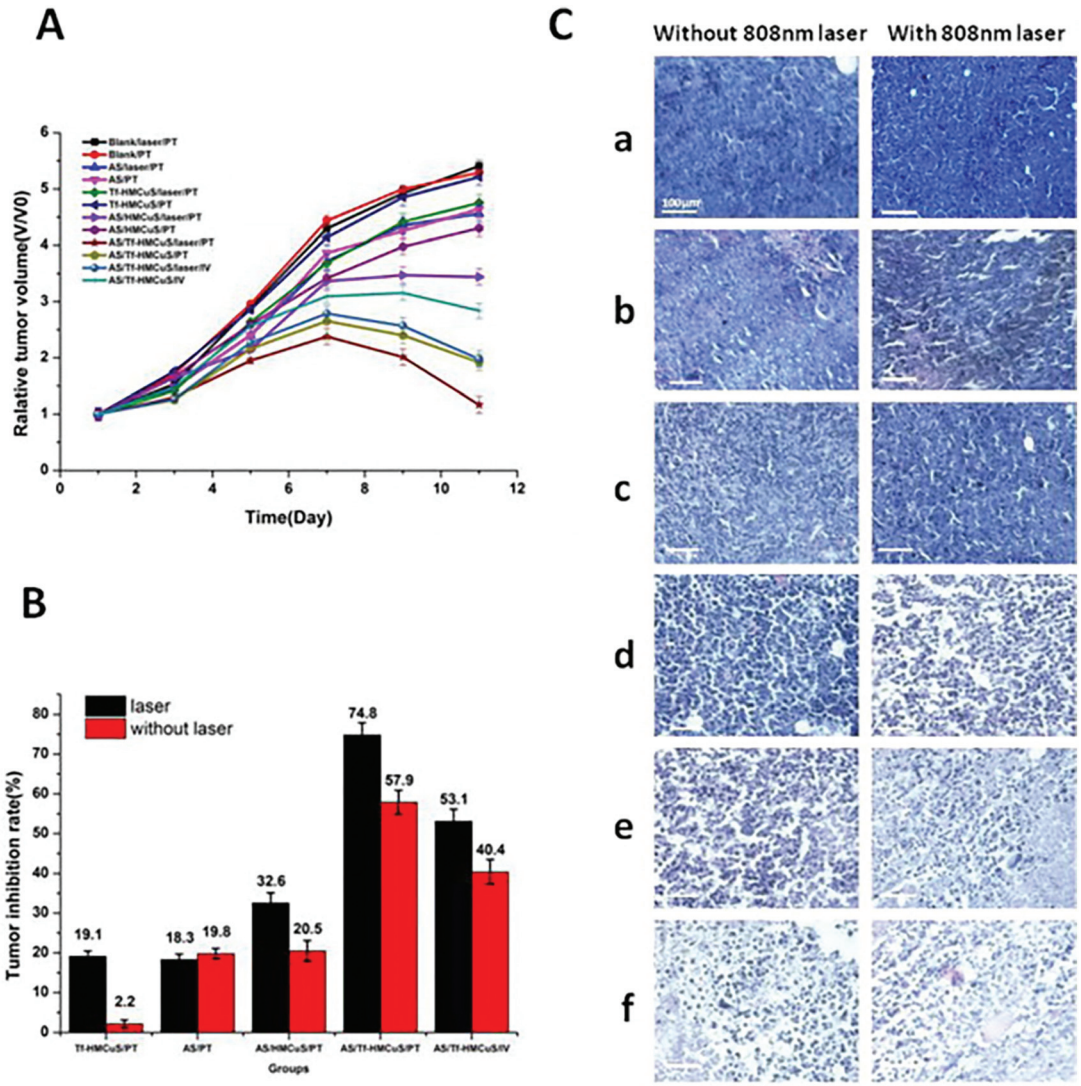

Fig. 8 Antitumor activity of artesunate-loaded hollow porous copper sulfide nanoparticles. Analysis of the tumor volume (A) and tumor inhibition (B) after treatment with different hollow porous copper sulfide nanoformulations and irradiation with the NIR laser (808 nm, 2 W cm^{-2}). Histological images of H&E stained tumor samples (C) after treatment with the different porous copper sulfide nanoformulations. Reprinted from L. Hou, X. Shan, L. Hao, Q. Feng, Z. Zhang, Copper sulfide nanoparticle-based localized drug delivery system as an effective cancer synergistic treatment and theranostic platform, *Acta Biomater.*, **54**, 307–320, Copyright (2017), with permission from Elsevier.

demonstrated by the approaches based on hyperthermia mediated by nanomaterials, their translation into the clinic is still poorly investigated. In fact, most of the nanomaterial-mediated hyperthermia approaches under clinical development are based on the utilization of magnetic fields for promoting heat generation.[166]

For example, NanoTherm® (MagForce AG) is applied in the treatment of glioblastomas and consists of an aqueous suspension of FeO nanoparticles that produces heat in the presence of alternating magnetic fields.[167,168] The nanoparticles possess an average size from 10 to 15 nm and are injected into the tumor or in the cavity wall during the tumor resection. The FeO core (≈111 mg ml^{-1} Fe concentration) is coated with amino silanes to ensure that the nanoparticles remain stable in the tumor tissue. After reaching the tumor site, the iron oxide nanoparticles are activated by an external alternating magnetic field, for six one-hour sessions (magnetic hyperthermia). Thus, the tumor thermal ablation is performed, usually at temperatures ≈44–45 °C, which can also sensitize the cells to other therapeutic approaches such as chemotherapy or radiotherapy.[166,169] In fact, the efficacy of Nanotherm® shows improvements when combined with other therapies.[170,171] This approach was approved by the European Medicines Agency for the treatment of brain tumors and is currently under clinical investigation in the United States of America.[166]

Magnablate I is another iron oxide nanoparticle-based magnetic treatment under clinical trials for the treatment of prostate cancer.[172] A clinical phase 0 study (ClinicalTrials.gov Identifier: NCT02033447, data still not available) has been developed to test where the nanoparticles are located after the

Table 2 Overview of the inorganic nanoparticles (gold, tungsten, molybdenum, iron oxide, copper, carbon-based materials) and the effect of their surface modification on the biological performance (*i.e.* biodistribution, antitumor efficacy, and biocompatibility). (N.A.) not applicable; (N.D.) not disclosed

Material		Surface modification	Biodistribution	Antitumor efficacy	Biocompatibility	Ref.
Gold	Nanorods	PEG and rabies virus glycoprotein	At 12 h after administration, predominantly accumulated in the liver and kidney. No significant damage and inflammatory reactions detected in the major organs	Tumor eradication after 13 days (200 μL at 2.5×10^{-3} M)	0.02–0.10 mM of [Au]	176
		β-Cyclodextrin and RLA peptide	No significant damage and inflammatory reactions detected in the major organs	Inhibition of the tumor growth for 21 days (20 mg kg^{-1})	0–200 mg L^{-1}	178
		β-Cyclodextrin, lactobionic acid, and PEG	At 24 h after injection, 50% of nanoparticles accumulated in the tumor and 30% in the liver. Some vestiges on the spleen, kidney and heart. No significant damage and inflammatory reactions detected in the major organs.	Tumor eradication after 7 days (1.15 mg kg^{-1})	0–200 mg L^{-1}	180
		PEG	At 24 h after injection, 8.6% of the nanoparticles accumulated in the tumor, 25.1% in the spleen, 13.9% in the liver, and some vestiges on other organs. No significant damage and inflammatory reactions detected in the major organs	Reduction of the tumor volume after 14 days (150 μL at 2 mg mL^{-1})	50–1000 mg L^{-1}	182
	Nanostars	N.A.	After 48 h, 2.11% and 0.88% of the nanostars with 30 nm and 60 nm accumulated in the tumor, respectively. Nanostars with 60 nm presented higher accumulation in the liver (~19%) and spleen. No significant damage and inflammatory reactions detected in the major organs	Tumor ablation with a single 20 minutes laser treatment (2 mg of the nanoparticles)	N.D.	42
		PEG	High uptake from the liver, spleen and lung	Tumor eradication after 2 days (50 μL at 32 mM)	0–500 μg mL^{-1}	183
		PEG	After 24 h, 20% of the nanoparticles accumulated in the spleen; 15% in the liver and ≈2.5% in the tumor. No significant damage and inflammatory reactions detected in the major organs	Tumor eradication after 2 days (100 mL at 4 mg mL^{-1})	0–400 μg mL^{-1}	184
		FA	No significant damage and inflammatory reactions detected in the major organs	Reduction of the tumor volume (1.4 mg mL^{-1}). Tumor recurrence after 16 days	0–1 mM of [Au]	187
	Nanoshells	Anti-EGFR antibody conjugated thiol chitosan-layer	Predominant accumulation of the nanoparticles in the tumor tissue	Tumor eradication for 16 days (175 μg mL^{-1})	0–250 μg mL^{-1}	78
		Betulinic acid liposomes	No significant damage and inflammatory reactions detected in the major organs	Significant reduction of the tumor volume after 14 days (200 μL at 94.9 μg mL^{-1})	1.5–47.5 μg mL^{-1}	226
		PEGylated SN-38-micelles	No significant damage and inflammatory reactions detected in the major organs	Reduction of the tumor growth for 35 days (1 mg kg^{-1})	0.125–2 mM of [Au]	227
	Nanoclusters	Hybrid albumin	The liver, kidney, heart, lung, and spleen did not show significant histological damage	Reduction of the tumor volume for 20 days (200 μl at 10 mg mL^{-1})	0–100 μg mL^{-1}	76
		PEG	Heart cytotoxicity was detected	Tumor eradication (2.5 mg kg^{-1})	4–1024 μg mL^{-1}	228
		Captoril	No significant damage and inflammatory reactions detected in the major organs	Tumor eradication after 15 days (100 mL at 2.5 mg mL^{-1})	0–100 μg mL^{-1}	229
	Nanocages	PEI, FA and PEG	Predominant accumulation of the nanoparticles in the tumor tissue, followed by the spleen and liver. No significant damage and inflammatory reactions detected in the major organs	Inhibition of the tumor growth for 15 days (8.5 mg kg^{-1})	N.D.	90
		HA, PEG, and A54 peptide	No significant damage and inflammatory reactions detected in the major organs	Inhibition of the tumor growth for 13 days (32.6 mg kg^{-1})	0.625×10^{10}–5×10^{10} particles per mL	230
		Acylsulfonamide	High nanoparticle accumulation in the spleen and liver (15% and 20%, respectively) and around 10% in the tumor. No significant damage and inflammatory reactions detected in the major organs	Tumor eradication after 35 days (100 μL at 2.5 mg mL^{-1})	N.D.	231

Table 2 *(Contd.)*

Material		Surface modification	Biodistribution	Antitumor efficacy	Biocompatibility	Ref.
Tungsten	Oxide	HA	Predominant accumulation of the nanoparticles in the tumor tissue followed by the kidney, liver and lung	Tumor eradication after 20 days (30 mg kg^{-1})	0.001–1 mg mL^{-1}	48
		iRGD peptide	Predominant accumulation of the nanoparticles in the tumor tissue. No significant damage and inflammatory reactions detected in the major organs	Reduction of the tumor growth for 16 days (100 μL at 1 mg mL^{-1})	N.D.	136
		Polyallylamine hydrochloride and polystyrenesulfonate	Predominant accumulation of the nanoparticles in the liver followed by the kidney, lung, spleen, tumor and heart, after 14 days. No significant damage and inflammatory reactions detected in the major organs	Tumor eradication after 8 days (100 μL at 1 mg mL^{-1})	15.625–1000 μg mL^{-1}	133
		γ-Poly-L-glutamic acid	No significant damage and inflammatory reactions detected in the major organs	Reduction of the tumor volume for 18 days (20 mg kg^{-1})	12.5–200 μg mL^{-1}	137
	Disulfide	PEG	High nanoparticle accumulation in the tumor (13%) followed by the liver and spleen (40% and 30%, respectively). No significant damage and inflammatory reactions detected in the major organs for 45 days	Tumor eradication after 2 days (200 μL at 2 mg mL^{-1})	0–0.1 mg mL^{-1}	194
		BSA	N.D.	Tumor eradication after 14 days (100 mL at 200 mg mL^{-1})	0–400 μg mL^{-1}	195
		BSA	No significant damage and inflammatory reactions detected in the major organs	Tumor eradication after 22 days (20 μL at 2 mg mL^{-1})	0–200 μg mL^{-1}	197
Molybdenum	Oxide	PEG	Predominant accumulation of the nanoparticles in the liver, spleen, lung, and kidney after 12 h. Clearing of the nanoparticles in the following 2 days No significant damage and inflammatory reactions detected in the major organs for 30 days	Reduction of the tumor volume for 15 days (20 mg kg^{-1})	0–200 μg mL^{-1}	142
		PEG	No significant damage and inflammatory reactions detected in the major organs	Reduction of the tumor volume for 15 days (0.2 mg kg^{-1})	0–200 μg mL^{-1}	156
		PEG	Predominant accumulation of the nanoparticles in the liver, spleen, lung, and kidney after 24 h. No significant damage and inflammatory reactions detected in the major organs for 30 days	Tumor eradication after 16 days (20 mg kg^{-1})	0–100 μg mL^{-1}	150
		Pluronic-F127	No significant damage and inflammatory reactions detected in the major organs	Tumor eradication after 24 days (3 mg kg^{-1})	0–100 μg mL^{-1}	18
	Disulfide	PEG	No significant damage and inflammatory reactions detected in the major organs	Reduction of tumor growth (6.85 mg kg^{-1})	0.25–8 μg mL^{-1}	145
		PEI	Predominant accumulation of the nanoparticles in the liver and spleen. No significant damage and inflammatory reactions detected in the major organs	Inhibition of tumor growth for 20 days (0.1 mL at 2 mg mL^{-1})	0–100 μg mL^{-1}	199
		PEG	Predominant accumulation of the nanoparticles in the lung, with some accumulation in the liver and spleen. No significant damage and inflammatory reactions detected in the major organs 7 days post-injection	Reduction of the tumor volume for 13 days (50 μL, 1 mg mL^{-1})	6.25–200 μg mL^{-1}	204
		GSH	Predominant accumulation of the nanoparticles in the liver (15.7%) followed by spleen (6.9%), kidney, and tumor. No significant damage and inflammatory reactions detected in the major organs	Tumor eradication after 4 days (200 μL at 0.5 mg mL^{-1})	1.06–200 μg mL^{-1}	205

Table 2 *(Contd.)*

Material		Surface modification	Biodistribution	Antitumor efficacy	Biocompatibility	Ref.
Iron based	Oxide	PEG or citrate	N.D.	Tumor eradication after 2 days without recurrence in 20 days (200 μL at 0.25 mg mL^{-1})	5–1000 mg mL^{-1}	208
		Carboxymethyl chitosan	Predominant accumulation of the nanoparticles in the tumor followed by the liver, spleen, kidney, and lung. No significant damage and inflammatory reactions detected in the major organs	Tumor eradication after 5 days without recurrence in 15 days (200 mL at 10 mg mL^{-1})	0–120 μg mL^{-1}	211
		Polydopamine	No significant damage and inflammatory reactions detected in the major organs	Reduction of the tumor volume for 19 days (25 μL at 2 mg mL^{-1})	0–400 μg mL^{-1}	212
		N.A.	N.D.	Reduction of tumor growth for 19 days (25 μL at 2 mg mL^{-1})	0–500 μg mL^{-1}	213
Copper	Seline	Dimercapto PEG	Predominant accumulation of the nanoparticles in the liver, spleen, kidney and lung after 24 h. No significant damage and inflammatory reactions detected in the major organs	Tumor eradication after 2 days (200 μL at 100 μg mL^{-1})	6.25–100 μg mL^{-1}	218
		N.A.	No significant damage and inflammatory reactions detected in the major organs	Reduction of tumor growth for 11 days (50 mg kg^{-1})	1.6–50 μg mL^{-1}	220
		N.A.	Similar accumulation of the nanoparticles in the heart, liver, spleen, and lungs. No significant damage and inflammatory reactions detected in the major organs after 3, 30, and 90 days	Tumor eradication after 14 days (200 mL at 1 mg mL^{-1})	0–100 ppm	222
	Sulfide	DSPE-PEG2000	Predominant accumulation of the nanoparticles in the liver followed by the spleen, kidney, heart and tumor. No significant damage and inflammatory reactions detected in the major organs	Tumor eradication after 14 days (200 μL at 1 mg mL^{-1})	0–400 ppm	217
Carbon based	Multi-walled carbon nanotubes functionalized with PEG	PEG	Predominant accumulation of the nanoparticles in the liver followed by the spleen, and kidney after 24 h. No significant damage and inflammatory reactions detected in the major organs	Tumor eradication after 12 days (4 mg kg^{-1})	N.D.	113
	Single-walled carbon nanotubes	Albumin	N.D.	Tumor eradication after 16 days (3 mg kg^{-1})	0.001–50 mM	103
	Single-walled carbon nanotubes	HA	No significant damage and inflammatory reactions detected in the major organs	Tumor eradication after 3 days (2.72 mg kg^{-1})	0–500 μg mL^{-1}	102
	Multifunctional carbon dots	PEG	N.D.	Inhibition of tumor growth for 11 days (4.0 mg kg^{-1})	0.2–2 μg mL^{-1}	97
	Go and rGO	Coated gold superparticles	N.D.	Tumor eradication after 14 days (200 μL at 1 mg mL^{-1})	0–200 μg ml^{-1}	116
		N.A.	Predominant accumulation of the nanoparticles in the liver, kidney and lung after 4 h	Reduction of tumor growth for 21 days (2.5 mg kg^{-1})	50–500 μg ml^{-1}	225
		Polydopamine	No significant damage and inflammatory reactions detected in the major organs	Tumor eradication after 18 days (200 μL at 20 mg L^{-1})	2.5–40 μg ml^{-1}	94
		N.A.	N.D.	Tumor eradication after 17 days (50 μL at 6 mg mL^{-1})	0–160 μg ml^{-1}	96

intratumoral injection and if any prostate-related side effects or irreversible damage can occur. Otherwise, Aurolase® (Nanospectra) remains as the unique nanoparticle under clinical evaluation for the PTT of cancer.[173] In fact, two clinical trials are currently being performed using this technology, a study to evaluate the efficacy of the Aurolase® therapeutic approach in primary and/or metastatic lung tumors (ClinicalTrials.gov Identifier: NCT01679470) and the determination of the antitumoral capacity in patients with refractory and/or recurrent tumors of the head and neck (ClinicalTrials.gov Identifier: NCT00848042).

Aurolase® uses PEGylated gold nanoshells with a diameter of approximately 150 nm and exhibits a high absorption peak at 800 nm, which allows its application in PTT. When the nanoparticles are intravenously injected, they explore the EPR effect to passively accumulate in the tumor site. The posterior NIR laser radiation may result in cellular death and tumor regression.[169,174] In the first clinical trial (ClinicalTrials.gov Identifier: NCT01679470), a single dose of gold nanoparticles was administered in patients with primary and/or metastatic tumors of the lung (with airway obstruction). Then, the PTT effect was triggered *via* bronchoscopy using optical fiber emitting NIR light (testing the irradiation of an escalating dose).[174,175] In the second PTT Aurolase® clinical study, patients with acute and/or chronic neck and head tumours received a single dose of gold nanoparticles through intravenous administration and were subjected to one or multiple doses of laser irradiation (808 nm). Three groups of 5 patients each, testing variations in the laser's power density, were studied and monitored during 6 months after treatment. Both clinical trials were already completed in 2014, but results have not yet been published (ClinicalTrials.gov Identifier: NCT00848042).[174,175]

4. Conclusion

Over the last few years, the utilization of nanomaterial-mediated hyperthermia in cancer therapy has been showing promising results. In this field, a wide number of nanomaterials have been developed, particularly those that can mediate a localized hyperthermia in response to NIR light irradiation. These nanostructures are able to convert the energy of the photons into heat, which allows the spatiotemporal control over the therapeutic effect.

In this review, the main inorganic nanomaterials (*e.g.* gold, carbon, tungsten, molybdenum, iron, and copper) developed for mediating cancer PTT were described and their general properties were summarized. In general, the data available in the literature demonstrate that the photothermal capacity of these nanomaterials can be optimized by adjusting their size, shape and doping with other elements. Moreover, it is worth noting that the therapeutic efficacy of the nanomaterial-mediated PTT is also dependent on other external parameters such as tumor localization, NIR laser conditions (*e.g.* potency and irradiation time), and accumulation within the tumor tissue. Additionally, researchers must also take into consideration the relationship between the high photothermal efficiency and biosafety of the nanostructures. For instance, several works have explored the functionalization of nanomaterials with polymers (*e.g.* PEG) and targeting agents (*e.g.* Fa, antibodies, and RGD peptide) for improving the materials stability, biocompatibility, and specificity for tumors (Table 2). Furthermore, the integration of the photothermal effect in combinatorial therapies can further improve the therapeutic potential of these nanostructures, leading to a decrease of the dose required to attain the eradication of tumor cells and treatment side-effects.

In conclusion, the PTT mediated by nanomaterials holds potential for improving the therapeutic outcome of cancer. Nevertheless, most of these nanomaterials remain at the preclinical stage and additional studies to characterize the short- and long-term fate of the nanomaterials in the body, their biodegradation, and their safety are of paramount importance to prompt their translation from the lab to the clinic. Moreover, the development of simple production methods and their scale-up will increase the reproducibility of the nanomaterials and their therapeutic effects.

Conflicts of interest

The authors declare no financial or commercial conflict of interest.

Acknowledgements

This work was supported by FEDER funds through the POCI – COMPETE 2020 – Operational Programme Competitiveness and Internationalisation in Axis I – Strengthening research, technological development and innovation (Project POCI-01 0145-FEDER-007491) and National Funds by FCT – Foundation for Science and Technology (Project UID/Multi/00709/2013). The funding from CENTRO-01-0145-FEDER-028989 and POCI-01-0145-FEDER-031462 is also acknowledged. Carolina F. Rodrigues acknowledges her individual Ph.D fellowship from FCT (SFRH/BD/144680/2019). The funders had no role in the decision to publish or in the preparation of the manuscript.

References

1 F. Bray, *et al.*, Global cancer statistics 2018: GLOBOCAN estimates of incidence and mortality worldwide for 36 cancers in 185 countries, *CA-Cancer J. Clin.*, 2018, **68**(6), 394–424.
2 C. Liang, W. Chao and L. Zhuang, Functional nanomaterials for phototherapies of cancer, *Chin. J. Clin. Oncol.*, 2014, (1), 18–26.
3 N. Datta, *et al.*, Local hyperthermia combined with radiotherapy and-/or chemotherapy: Recent advances and

promises for the future, *Cancer Treat. Rev.*, 2015, **41**(9), 742–753.
4 D. M. Pardoll, The blockade of immune checkpoints in cancer immunotherapy, *Nat. Rev. Cancer*, 2012, **12**(4), 252–264.
5 C. A. Robertson, D. H. Evans and H. Abrahamse, Photodynamic therapy (PDT): a short review on cellular mechanisms and cancer research applications for PDT, *J. Photochem. Photobiol., B*, 2009, **96**(1), 1–8.
6 G. Kong and M. Dewhirst, Review hyperthermia and liposomes, *Int. J. Hyperthermia*, 1999, **15**(5), 345–370.
7 P. Wust, *et al.*, Hyperthermia in combined treatment of cancer, *Lancet Oncol.*, 2002, **3**(8), 487–497.
8 D. K. Chatterjee, P. Diagaradjane and S. Krishnan, Nanoparticle-mediated hyperthermia in cancer therapy, *Ther. Delivery*, 2011, **2**(8), 1001–1014.
9 J. Beik, *et al.*, Nanotechnology in hyperthermia cancer therapy: From fundamental principles to advanced applications, *J. Controlled Release*, 2016, **235**, 205–221.
10 C. S. Kumar and F. Mohammad, Magnetic nanomaterials for hyperthermia-based therapy and controlled drug delivery, *Adv. Drug Delivery Rev.*, 2011, **63**(9), 789–808.
11 D. de Melo-Diogo, *et al.*, Strategies to improve cancer photothermal therapy mediated by nanomaterials, *Adv. Healthcare Mater.*, 2017, **6**(10), 1700073.
12 A. F. Moreira, D. R. Dias and I. J. Correia, Stimuli-responsive mesoporous silica nanoparticles for cancer therapy: A review, *Microporous Mesoporous Mater.*, 2016, **236**, 141–157.
13 G. S. Terentyuk, *et al.*, Laser-induced tissue hyperthermia mediated by gold nanoparticles: toward cancer phototherapy, *J. Biomed. Opt.*, 2009, **14**(2), 021016.
14 R. Seip, C. T. Chin, C. S. Hall, B. I. Raju, A. Ghanem and K. Tiemann, Targeted Ultrasound-Mediated Delivery of Nanoparticles: On the Development of a New HIFU-Based Therapy and Imaging Device, in *IEEE Transactions on Biomedical Engineering*, 2010, vol. **57**, pp. 61–70.
15 I. M. Obaidat, B. Issa and Y. Haik, Magnetic properties of magnetic nanoparticles for efficient hyperthermia, *Nanomaterials*, 2015, **5**(1), 63–89.
16 A. M. Pekkanen, M. R. DeWitt and M. N. Rylander, Nanoparticle enhanced optical imaging and phototherapy of cancer, *J. Biomed. Nanotechnol.*, 2014, **10**(9), 1677–1712.
17 J. Zhou, *et al.*, NIR photothermal therapy using polyaniline nanoparticles, *Biomaterials*, 2013, **34**(37), 9584–9592.
18 Y. Chen, *et al.*, Pluronic F127-functionalized molybdenum oxide nanosheets with pH-dependent degradability for chemo-photothermal cancer therapy, *J. Colloid Interface Sci.*, 2019, **553**, 567–580.
19 H. Dong and Y. Cao, Carbon Nanomaterials for Optical Bioimaging and Phototherapy, *Carbon Nanomater. Bioimaging, Bioanal., Ther.*, 2019, 43–62.
20 J. Estelrich and M. A. Busquets, Iron oxide nanoparticles in photothermal therapy, *Molecules*, 2018, **23**(7), 1567.
21 A. F. Moreira, *et al.*, Gold-core silica shell nanoparticles application in imaging and therapy: A review, *Microporous Mesoporous Mater.*, 2018, **270**, 168–179.
22 S. Yin and Y. Asakura, Recent research progress on mixed valence state tungsten based materials, *Tungsten*, 2019, **1**(1), 5–18.
23 M. Zhou, M. Tian and C. Li, Copper-based nanomaterials for cancer imaging and therapy, *Bioconjugate Chem.*, 2016, **27**(5), 1188–1199.
24 X. Huang, *et al.*, *Gold nanoparticles: interesting optical properties and recent applications in cancer diagnostics and therapy*, 2007.
25 N. Li, P. Zhao and D. Astruc, Anisotropic gold nanoparticles: synthesis, properties, applications, and toxicity, *Angew. Chem., Int. Ed.*, 2014, **53**(7), 1756–1789.
26 K. Greish, Enhanced permeability and retention (EPR) effect for anticancer nanomedicine drug targeting, in *Cancer nanotechnology*, Springer, 2010, pp. 25–37.
27 J. Chen, *et al.*, Nanomaterials as photothermal therapeutic agents, *Prog. Mater. Sci.*, 2019, **99**, 1–26.
28 R. Singh and J. W. Lillard Jr., Nanoparticle-based targeted drug delivery, *Exp. Mol. Pathol.*, 2009, **86**(3), 215–223.
29 S. M. Moghimi, A. C. Hunter and J. C. Murray, Long-circulating and target-specific nanoparticles: theory to practice, *Pharmacol. Rev.*, 2001, **53**(2), 283–318.
30 B. Wang, *et al.*, Metabolism of nanomaterials in vivo: blood circulation and organ clearance, *Acc. Chem. Res.*, 2013, **46**(3), 761–769.
31 R. K. Jain and T. Stylianopoulos, Delivering nanomedicine to solid tumors, *Nat. Rev. Clin. Oncol.*, 2010, **7**(11), 653.
32 Y. Matsumoto, *et al.*, Vascular bursts enhance permeability of tumour blood vessels and improve nanoparticle delivery, *Nat. Nanotechnol.*, 2016, **11**(6), 533.
33 A. Lamprecht, *et al.*, Biodegradable nanoparticles for targeted drug delivery in treatment of inflammatory bowel disease, *J. Pharmacol. Exp. Ther.*, 2001, **299**(2), 775–781.
34 D. N. Heo, *et al.*, Gold nanoparticles surface-functionalized with paclitaxel drug and biotin receptor as theranostic agents for cancer therapy, *Biomaterials*, 2012, **33**(3), 856–866.
35 U. Chitgupi, Y. Qin and J. F. Lovell, Targeted nanomaterials for phototherapy, *Nanotheranostics*, 2017, **1**(1), 38.
36 S. Sunoqrot, *et al.*, Prolonged blood circulation and enhanced tumor accumulation of folate-targeted dendrimer-polymer hybrid nanoparticles, *J. Controlled Release*, 2014, **191**, 115–122.
37 J.-W. Yoo, E. Chambers and S. Mitragotri, Factors that control the circulation time of nanoparticles in blood: challenges, solutions and future prospects, *Curr. Pharm. Des.*, 2010, **16**(21), 2298–2307.
38 B.-J. L. Van Hong Nguyen, Protein corona: a new approach for nanomedicine design, *Int. J. Nanomed.*, 2017, **12**, 3137.
39 A. E. Nel, *et al.*, Understanding biophysicochemical interactions at the nano–bio interface, *Nat. Mater.*, 2009, **8**(7), 543–557.
40 X. Li, *et al.*, The systematic evaluation of size-dependent toxicity and multi-time biodistribution of gold nanoparticles, *Colloids Surf., B*, 2018, **167**, 260–266.

41 E. K. Larsen, *et al.*, Size-dependent accumulation of PEGylated silane-coated magnetic iron oxide nanoparticles in murine tumors, *ACS Nano*, 2009, **3**(7), 1947–1951.
42 Y. Liu, *et al.*, A plasmonic gold nanostar theranostic probe for in vivo tumor imaging and photothermal therapy, *Theranostics*, 2015, **5**(9), 946.
43 S. D. Perrault, *et al.*, Mediating tumor targeting efficiency of nanoparticles through design, *Nano Lett.*, 2009, **9**(5), 1909–1915.
44 M. J. Ernsting, *et al.*, Factors controlling the pharmacokinetics, biodistribution and intratumoral penetration of nanoparticles, *J. Controlled Release*, 2013, **172**(3), 782–794.
45 S.-D. Li and L. Huang, Pharmacokinetics and biodistribution of nanoparticles, *Mol. Pharm.*, 2008, **5**(4), 496–504.
46 S.-D. Li and L. Huang, Nanoparticles evading the reticuloendothelial system: role of the supported bilayer, *Biochim. Biophys. Acta, Biomembr.*, 2009, **1788**(10), 2259–2266.
47 M. Wang and M. Thanou, Targeting nanoparticles to cancer, *Pharmacol. Res.*, 2010, **62**(2), 90–99.
48 S. M. Sharker, *et al.*, Functionalized biocompatible WO3 nanoparticles for triggered and targeted in vitro and in vivo photothermal therapy, *J. Controlled Release*, 2015, **217**, 211–220.
49 M. Xuan, *et al.*, Macrophage cell membrane camouflaged Au nanoshells for in vivo prolonged circulation life and enhanced cancer photothermal therapy, *ACS Appl. Mater. Interfaces*, 2016, **8**(15), 9610–9618.
50 C. F. Rodrigues, *et al.*, Functionalization of AuMSS nanorods towards more effective cancer therapies, *Nano Res.*, 2019, **12**(4), 719–732.
51 V. Amendola, *et al.*, Surface plasmon resonance in gold nanoparticles: a review, *J. Phys.: Condens. Matter*, 2017, **29**(20), 203002.
52 D. Jaque, *et al.*, Nanoparticles for photothermal therapies, *Nanoscale*, 2014, **6**(16), 9494–9530.
53 J.-L. Li and M. Gu, Gold-nanoparticle-enhanced cancer photothermal therapy, *IEEE J. Sel. Top. Quantum Electron.*, 2009, **16**(4), 989–996.
54 X. Huang, *et al.*, Plasmonic photothermal therapy (PPTT) using gold nanoparticles, *Lasers Med. Sci.*, 2008, **23**(3), 217.
55 A. F. Bagley, *et al.*, Plasmonic photothermal heating of intraperitoneal tumors through the use of an implanted near-infrared source, *ACS Nano*, 2013, **7**(9), 8089–8097.
56 D. de Melo-Diogo, *et al.*, Strategies to Improve Cancer Photothermal Therapy Mediated by Nanomaterials, *Adv. Healthcare Mater.*, 2017, **6**(10), 1700073.
57 A. F. Moreira, *et al.*, Poly (vinyl alcohol)/chitosan layer-by-layer microneedles for cancer chemo-photothermal therapy, *Int. J. Pharm.*, 2020, **576**, 118907.
58 C. F. Rodrigues, *et al.*, Optimization of gold core-mesoporous silica shell functionalization with TPGS and PEI for cancer therapy, *Microporous Mesoporous Mater.*, 2019, **285**, 1–12.
59 C. Yao, *et al.*, Gold nanoparticle mediated phototherapy for cancer, *J. Nanomater.*, 2016, **2016**, 1–29.
60 A. Amendoeira, *et al.*, Light Irradiation of Gold Nanoparticles Toward Advanced Cancer Therapeutics, *Adv. Ther.*, 2020, **3**(1), 1900153.
61 T. S. Lopes, *et al.*, Advances and potential application of gold nanoparticles in nanomedicine, *J. Cell. Biochem.*, 2019, **120**(10), 16370–16378.
62 P. Zhao, N. Li and D. Astruc, State of the art in gold nanoparticle synthesis, *Coord. Chem. Rev.*, 2013, **257**(3–4), 638–665.
63 C. A. Reis, *et al.*, Development of gold-core silica shell nanospheres coated with poly-2-ethyl-oxazoline and β-cyclodextrin aimed for cancer therapy, *Mater. Sci. Eng., C*, 2019, **98**, 960–968.
64 Y. Xia and N. J. Halas, Shape-controlled synthesis and surface plasmonic properties of metallic nanostructures, *MRS Bull.*, 2005, **30**(5), 338–348.
65 I. Blakey, Z. Merican and K. J. Thurecht, A method for controlling the aggregation of gold nanoparticles: tuning of optical and spectroscopic properties, *Langmuir*, 2013, **29**(26), 8266–8274.
66 S. Link and M. A. El-Sayed, Size and temperature dependence of the plasmon absorption of colloidal gold nanoparticles, *J. Phys. Chem. B*, 1999, **103**(21), 4212–4217.
67 S. Link and M. A. El-Sayed, *Spectral properties and relaxation dynamics of surface plasmon electronic oscillations in gold and silver nanodots and nanorods*, ACS Publications, 1999.
68 P. K. Jain, I. H. El-Sayed and M. A. El-Sayed, Au nanoparticles target cancer, *Nano Today*, 2007, **2**(1), 18–29.
69 Y. Sun and Y. Xia, Gold and silver nanoparticles: a class of chromophores with colors tunable in the range from 400 to 750 nm, *Analyst*, 2003, **128**(6), 686–691.
70 B. M. Reinhard, *et al.*, Calibration of dynamic molecular rulers based on plasmon coupling between gold nanoparticles, *Nano Lett.*, 2005, **5**(11), 2246–2252.
71 P. K. Jain, W. Huang and M. A. El-Sayed, On the universal scaling behavior of the distance decay of plasmon coupling in metal nanoparticle pairs: a plasmon ruler equation, *Nano Lett.*, 2007, **7**(7), 2080–2088.
72 P. K. Jain and M. A. El-Sayed, Universal scaling of plasmon coupling in metal nanostructures: extension from particle pairs to nanoshells, *Nano Lett.*, 2007, **7**(9), 2854–2858.
73 J. P. Kottmann and O. J. Martin, Plasmon resonant coupling in metallic nanowires, *Opt. Express*, 2001, **8**(12), 655–663.
74 L. Sweatlock, *et al.*, Highly confined electromagnetic fields in arrays of strongly coupled Ag nanoparticles, *Phys. Rev. B: Condens. Matter Mater. Phys.*, 2005, **71**(23), 235408.
75 H. Li, *et al.*, Combination of active targeting, enzyme-triggered release and fluorescent dye into gold nanoclusters for endomicroscopy-guided photothermal/photodynamic therapy to pancreatic ductal adenocarcinoma, *Biomaterials*, 2017, **139**, 30–38.

76 S. Park, *et al.*, Gold nanocluster-loaded hybrid albumin nanoparticles with fluorescence-based optical visualization and photothermal conversion for tumor detection/ablation, *J. Controlled Release*, 2019, **304**, 7–18.
77 M. Wang, *et al.*, Gold nanoshell coated thermo-pH dual responsive liposomes for resveratrol delivery and chemo-photothermal synergistic cancer therapy, *J. Mater. Chem. B*, 2017, **5**(11), 2161–2171.
78 P. Manivasagan, *et al.*, Anti-EGFR antibody conjugated thiol chitosan-layered gold nanoshells for dual-modal imaging-guided cancer combination therapy, *J. Controlled Release*, 2019, **311**, 26–42.
79 A. Ben-Yakar, D. Eversole and O. Ekici, Spherical and anisotropic gold nanomaterials in plasmonic laser phototherapy of cancer, in *Nanotechnologies for the Life Sciences: Online*, 2007.
80 K.-S. Lee and M. A. El-Sayed, Dependence of the enhanced optical scattering efficiency relative to that of absorption for gold metal nanorods on aspect ratio, size, end-cap shape, and medium refractive index, *J. Phys. Chem. B*, 2005, **109**(43), 20331–20338.
81 X. Huang and M. A. El-Sayed, Gold nanoparticles: Optical properties and implementations in cancer diagnosis and photothermal therapy, *J. Adv. Res.*, 2010, **1**(1), 13–28.
82 M. A. Mackey, *et al.*, The most effective gold nanorod size for plasmonic photothermal therapy: theory and in vitro experiments, *J. Phys. Chem. B*, 2014, **118**(5), 1319–1326.
83 W. Zhang, *et al.*, pH and near-infrared light dual-stimuli responsive drug delivery using DNA-conjugated gold nanorods for effective treatment of multidrug resistant cancer cells, *J. Controlled Release*, 2016, **232**, 9–19.
84 S. Barbosa, *et al.*, Tuning size and sensing properties in colloidal gold nanostars, *Langmuir*, 2010, **26**(18), 14943–14950.
85 C. G. Khoury and T. Vo-Dinh, Gold nanostars for surface-enhanced Raman scattering: synthesis, characterization and optimization, *J. Phys. Chem. C*, 2008, **112**(48), 18849–18859.
86 A. Espinosa, *et al.*, Cancer cell internalization of gold nanostars impacts their photothermal efficiency in vitro and in vivo: toward a plasmonic thermal fingerprint in tumoral environment, *Adv. Healthcare Mater.*, 2016, **5**(9), 1040–1048.
87 F. Xia, *et al.*, Matrix metallopeptidase 2 targeted delivery of gold nanostars decorated with IR-780 iodide for dual-modal imaging and enhanced photothermal/photodynamic therapy, *Acta Biomater.*, 2019, **89**, 289–299.
88 Y. Feng, *et al.*, Time-staggered delivery of erlotinib and doxorubicin by gold nanocages with two smart polymers for reprogrammable release and synergistic with photothermal therapy, *Biomaterials*, 2019, **217**, 119327.
89 J. Chen, *et al.*, Gold nanocages: bioconjugation and their potential use as optical imaging contrast agents, *Nano Lett.*, 2005, **5**(3), 473–477.
90 S. Huang, *et al.*, Folic-Acid-Mediated Functionalized Gold Nanocages for Targeted Delivery of Anti-miR-181b in Combination of Gene Therapy and Photothermal Therapy against Hepatocellular Carcinoma, *Adv. Funct. Mater.*, 2016, **26**(15), 2532–2544.
91 H. Sun, *et al.*, Cancer cell membrane-coated gold nanocages with hyperthermia-triggered drug release and homotypic target inhibit growth and metastasis of breast cancer, *Adv. Funct. Mater.*, 2017, **27**(3), 1604300.
92 P. Jeyamohan, *et al.*, Accelerated killing of cancer cells using a multifunctional single-walled carbon nanotube-based system for targeted drug delivery in combination with photothermal therapy, *Int. J. Nanomed.*, 2013, **8**, 2653.
93 H. Wang, *et al.*, Biocompatible chitosan–carbon dot hybrid nanogels for NIR-imaging-guided synergistic photothermal–chemo therapy, *ACS Appl. Mater. Interfaces*, 2017, **9**(22), 18639–18649.
94 D. Hu, *et al.*, Indocyanine green-loaded polydopamine-reduced graphene oxide nanocomposites with amplifying photoacoustic and photothermal effects for cancer theranostics, *Theranostics*, 2016, **6**(7), 1043.
95 B. Han, *et al.*, Carbon-Based Photothermal Actuators, *Adv. Funct. Mater.*, 2018, **28**(40), 1802235.
96 J. Yu, *et al.*, Improved anticancer photothermal therapy using the bystander effect enhanced by antiarrhythmic peptide conjugated dopamine-modified reduced graphene oxide nanocomposite, *Adv. Healthcare Mater.*, 2017, **6**(2), 1600804.
97 M. Zheng, *et al.*, One-pot to synthesize multifunctional carbon dots for near infrared fluorescence imaging and photothermal cancer therapy, *ACS Appl. Mater. Interfaces*, 2016, **8**(36), 23533–23541.
98 G. Fugallo, *et al.*, Thermal conductivity of graphene and graphite: collective excitations and mean free paths, *Nano Lett.*, 2014, **14**(11), 6109–6114.
99 A. A. Balandin, Thermal properties of graphene and nanostructured carbon materials, *Nat. Mater.*, 2011, **10**(8), 569–581.
100 S. Iijima, Helical microtubules of graphitic carbon, *Nature*, 1991, **354**(6348), 56–58.
101 R. Singh and S. V. Torti, Carbon nanotubes in hyperthermia therapy, *Adv. Drug Delivery Rev.*, 2013, **65**(15), 2045–2060.
102 G. Wang, *et al.*, Nanotubes-embedded indocyanine green–hyaluronic acid nanoparticles for photoacoustic-imaging-guided phototherapy, *ACS Appl. Mater. Interfaces*, 2016, **8**(8), 5608–5617.
103 L. Zhang, *et al.*, A novel single walled carbon nanotube (SWCNT) functionalization agent facilitating in vivo combined chemo/thermo therapy, *Nanoscale*, 2015, **7**(39), 16204–16213.
104 S. Augustine, *et al.*, Recent advances in carbon based nanosystems for cancer theranostics, *Biomater. Sci.*, 2017, **5**(5), 901–952.
105 C. Cha, *et al.*, Carbon-based nanomaterials: multifunctional materials for biomedical engineering, *ACS Nano*, 2013, **7**(4), 2891–2897.

106 C. Iancu, *et al.*, Enhanced laser thermal ablation for the in vitro treatment of liver cancer by specific delivery of multiwalled carbon nanotubes functionalized with human serum albumin, *Int. J. Nanomed.*, 2011, **6**, 129.
107 L. Xie, *et al.*, Functional long circulating single walled carbon nanotubes for fluorescent/photoacoustic imaging-guided enhanced phototherapy, *Biomaterials*, 2016, **103**, 219–228.
108 A. Aqel, *et al.*, Carbon nanotubes, science and technology part (I) structure, synthesis and characterisation, *Arabian J. Chem.*, 2012, **5**(1), 1–23.
109 B. Liu, *et al.*, Chirality-controlled synthesis and applications of single-wall carbon nanotubes, *ACS Nano*, 2017, **11**(1), 31–53.
110 J. Prasek, *et al.*, Methods for carbon nanotubes synthesis, *J. Mater. Chem.*, 2011, **21**(40), 15872–15884.
111 F. Wang, *et al.*, The optical resonances in carbon nanotubes arise from excitons, *Science*, 2005, **308**(5723), 838–841.
112 E. J. Comparetti, V. d. A. Pedrosa and R. Kaneno, Carbon nanotube as a tool for fighting cancer, *Bioconjugate Chem.*, 2017, **29**(3), 709–718.
113 B. Zhang, *et al.*, Fibrin-targeting peptide CREKA-conjugated multi-walled carbon nanotubes for self-amplified photothermal therapy of tumor, *Biomaterials*, 2016, **79**, 46–55.
114 I. Marangon, *et al.*, Synergic mechanisms of photothermal and photodynamic therapies mediated by photosensitizer/carbon nanotube complexes, *Carbon*, 2016, **97**, 110–123.
115 D. Wang, *et al.*, Facile preparation of doxorubicin-loaded and folic acid-conjugated carbon nanotubes@ poly (N-vinyl pyrrole) for targeted synergistic chemo–Photothermal Cancer treatment, *Bioconjugate Chem.*, 2017, **28**(11), 2815–2822.
116 L.-S. Lin, *et al.*, Dual-enhanced photothermal conversion properties of reduced graphene oxide-coated gold superparticles for light-triggered acoustic and thermal theranostics, *Nanoscale*, 2016, **8**(4), 2116–2122.
117 S. Gao, *et al.*, Hybrid graphene/Au activatable theranostic agent for multimodalities imaging guided enhanced photothermal therapy, *Biomaterials*, 2016, **79**, 36–45.
118 D. de Melo-Diogo, *et al.*, POxylated graphene oxide nanomaterials for combination chemo-phototherapy of breast cancer cells, *Eur. J. Pharm. Biopharm.*, 2018, **131**, 162–169.
119 O. C. Compton and S. T. Nguyen, Graphene oxide, highly reduced graphene oxide, and graphene: versatile building blocks for carbon-based materials, *Small*, 2010, **6**(6), 711–723.
120 B. Zhang, Y. Wang and G. Zhai, Biomedical applications of the graphene-based materials, *Mater. Sci. Eng., C*, 2016, **61**, 953–964.
121 C. Chung, *et al.*, Biomedical applications of graphene and graphene oxide, *Acc. Chem. Res.*, 2013, **46**(10), 2211–2224.
122 S. C. Ray, Application and uses of graphene oxide and reduced graphene oxide, in *Applications of Graphene and Graphene-Oxide Based Nanomaterials*, 2015, pp. 39–55.
123 J. T. Robinson, *et al.*, Ultrasmall reduced graphene oxide with high near-infrared absorbance for photothermal therapy, *J. Am. Chem. Soc.*, 2011, **133**(17), 6825–6831.
124 R. Lima-Sousa, *et al.*, Hyaluronic acid functionalized green reduced graphene oxide for targeted cancer photothermal therapy, *Carbohydr. Polym.*, 2018, **200**, 93–99.
125 Y. A. Cheon, J. H. Bae and B. G. Chung, Reduced graphene oxide nanosheet for chemo-photothermal therapy, *Langmuir*, 2016, **32**(11), 2731–2736.
126 S. Roy, A. Sarkar and A. Jaiswal, Poly (allylamine hydrochloride)-functionalized reduced graphene oxide for synergistic chemo-photothermal therapy, *Nanomedicine*, 2019, **14**(3), 255–274.
127 J. Li, *et al.*, Synthesis of monoclinic WO3 nanosphere hydrogen gasochromic film via a sol–gel approach using PS-b-PAA diblock copolymer as template, *Solid State Sci.*, 2010, **12**(8), 1393–1398.
128 N. Shankar, *et al.*, Synthesis of tungsten oxide (WO3) nanorods using carbon nanotubes as templates by hot filament chemical vapor deposition, *Mater. Lett.*, 2006, **60**(6), 771–774.
129 C. Balázsi, *et al.*, Nanosize hexagonal tungsten oxide for gas sensing applications, *J. Eur. Ceram. Soc.*, 2008, **28**(5), 913–917.
130 R. Huirache-Acuña, *et al.*, Synthesis and characterization of WO3 nanostructures prepared by an aged-hydrothermal method, *Mater. Charact.*, 2009, **60**(9), 932–937.
131 B. Bhuyan, *et al.*, Facile hydrothermal synthesis of ultrasmall W18O49 nanoparticles and studies of their photocatalytic activity towards degradation of methylene blue, *Mater. Chem. Phys.*, 2017, **188**, 1–7.
132 K. Manthiram and A. P. Alivisatos, Tunable localized surface plasmon resonances in tungsten oxide nanocrystals, *J. Am. Chem. Soc.*, 2012, **134**(9), 3995–3998.
133 W. Guo, *et al.*, CsxWO3 nanorods coated with polyelectrolyte multilayers as a multifunctional nanomaterial for bimodal imaging-guided photothermal/photodynamic cancer treatment, *Adv. Mater.*, 2017, **29**(4), 1604157.
134 S. Ghosh, *et al.*, Fabrication of tungsten nanocrystals and silver–tungsten nanonets: a potent reductive catalyst, *RSC Adv.*, 2015, **5**(49), 38971–38976.
135 H. Zuo, *et al.*, Platelet-mimicking nanoparticles co-loaded with W18O49 and metformin alleviate tumor hypoxia for enhanced photodynamic therapy and photothermal therapy, *Acta Biomater.*, 2018, **80**, 296–307.
136 Z. Yang, *et al.*, Tumor-Targeting W18O49 Nanoparticles for Dual-Modality Imaging and Guided Heat-Shock-Response-Inhibited Photothermal Therapy in Gastric Cancer, *Part. Part. Syst. Charact.*, 2019, **36**(7), 1900124.
137 P. Liu, *et al.*, Ultrasmall WO_{3-x}@ γ-poly-l-glutamic Acid Nanoparticles as a Photoacoustic Imaging and Effective Photothermal-Enhanced Chemodynamic Therapy Agent for Cancer, *ACS Appl. Mater. Interfaces*, 2018, **10**(45), 38833–38844.
138 F.-P. Koffyberg, K. Dwight and A. Wold, Interband transitions of semiconducting oxides determined from photo-

electrolysis spectra, *Solid State Commun.*, 1979, **30**(7), 433–437.
139 H. Zheng, *et al.*, Nanostructured tungsten oxide–properties, synthesis, and applications, *Adv. Funct. Mater.*, 2011, **21**(12), 2175–2196.
140 Y. Tian, *et al.*, Lentinan *in situ* coated tungsten oxide nanorods as a nanotherapeutic agent for low power density photothermal cancer therapy, *Int. J. Biol. Macromol.*, 2019, **137**, 904–911.
141 Z. Zhou, *et al.*, Tungsten oxide nanorods: an efficient nanoplatform for tumor CT imaging and photothermal therapy, *Sci. Rep.*, 2014, **4**, 3653.
142 W. Yin, *et al.*, Biodegradable MoO x nanoparticles with efficient near-infrared photothermal and photodynamic synergetic cancer therapy at the second biological window, *Nanoscale*, 2018, **10**(3), 1517–1531.
143 A. H. Odda, *et al.*, Plasmonic MoO_{3-x} nanoparticles incorporated in Prussian blue frameworks exhibit highly efficient dual photothermal/photodynamic therapy, *J. Mater. Chem. B*, 2019, **7**(12), 2032–2042.
144 H. Yang, *et al.*, Molybdenum oxide nano-dumplings with excellent stability for photothermal cancer therapy and as a controlled release hydrogel, *New J. Chem.*, 2019, **43**(36), 14281–14290.
145 T. Liu, *et al.*, Combined photothermal and photodynamic therapy delivered by PEGylated MoS2 nanosheets, *Nanoscale*, 2014, **6**(19), 11219–11225.
146 Y. Zhan, *et al.*, Phase-controlled synthesis of molybdenum oxide nanoparticles for surface enhanced Raman scattering and photothermal therapy, *Nanoscale*, 2018, **10**(13), 5997–6004.
147 L. Yuwen, *et al.*, Aqueous phase preparation of ultrasmall MoSe 2 nanodots for efficient photothermal therapy of cancer cells, *Nanoscale*, 2016, **8**(5), 2720–2726.
148 C. Rao, H. Ramakrishna Matte and U. Maitra, Graphene analogues of inorganic layered materials, *Angew. Chem., Int. Ed.*, 2013, **52**(50), 13162–13185.
149 D. Ding, *et al.*, MoO_{3-x} quantum dots for photoacoustic imaging guided photothermal/photodynamic cancer treatment, *Nanoscale*, 2017, **9**(5), 2020–2029.
150 G. Song, *et al.*, Degradable molybdenum oxide nanosheets with rapid clearance and efficient tumor homing capabilities as a therapeutic nanoplatform, *Angew. Chem., Int. Ed.*, 2016, **55**(6), 2122–2126.
151 V. Yadav, *et al.*, 2D MoS2-based nanomaterials for therapeutic, bioimaging, and biosensing applications, *Small*, 2019, **15**(1), 1803706.
152 T. Liu, *et al.*, Drug delivery with PEGylated MoS2 nanosheets for combined photothermal and chemotherapy of cancer, *Adv. Mater.*, 2014, **26**(21), 3433–3440.
153 K. Wang, *et al.*, Combined chemo-photothermal antitumor therapy using molybdenum disulfide modified with hyperbranched polyglycidyl, *ACS Biomater. Sci. Eng.*, 2017, **3**(10), 2325–2335.
154 I. A. de Castro, *et al.*, Molybdenum oxides–from fundamentals to functionality, *Adv. Mater.*, 2017, **29**(40), 1701619.
155 W. Liu, *et al.*, Highly stable molybdenum dioxide nanoparticles with strong plasmon resonance are promising in photothermal cancer therapy, *Biomaterials*, 2018, **163**, 43–54.
156 T. Bao, *et al.*, One-pot synthesis of PEGylated plasmonic MoO_{3-x} hollow nanospheres for photoacoustic imaging guided chemo-photothermal combinational therapy of cancer, *Biomaterials*, 2016, **76**, 11–24.
157 M. Saeed, W. Ren and A. Wu, Therapeutic applications of iron oxide based nanoparticles in cancer: basic concepts and recent advances, *Biomater. Sci.*, 2018, **6**(4), 708–725.
158 W. Wu, *et al.*, Recent progress on magnetic iron oxide nanoparticles: synthesis, surface functional strategies and biomedical applications, *Sci. Technol. Adv. Mater.*, 2015, **16**(2), 023501.
159 Y. Hu, *et al.*, Multifunctional porous iron oxide nanoagents for MRI and photothermal/chemo synergistic therapy, *Bioconjugate Chem.*, 2018, **29**(4), 1283–1290.
160 R.-M. Yang, *et al.*, Hyaluronan-modified superparamagnetic iron oxide nanoparticles for bimodal breast cancer imaging and photothermal therapy, *Int. J. Nanomed.*, 2017, **12**, 197.
161 M. B. Gawande, *et al.*, Cu and Cu-based nanoparticles: synthesis and applications in catalysis, *Chem. Rev.*, 2016, **116**(6), 3722–3811.
162 Y. Li, *et al.*, Copper sulfide nanoparticles for photothermal ablation of tumor cells, *Nanomedicine*, 2010, **5**(8), 1161–1171.
163 L. Hou, *et al.*, Copper sulfide nanoparticle-based localized drug delivery system as an effective cancer synergistic treatment and theranostic platform, *Acta Biomater.*, 2017, **54**, 307–320.
164 D. Wang, *et al.*, Erythrocyte–cancer hybrid membrane camouflaged hollow copper sulfide nanoparticles for prolonged circulation life and homotypic-targeting photothermal/chemotherapy of melanoma, *ACS Nano*, 2018, **12**(6), 5241–5252.
165 A. C. Anselmo and S. Mitragotri, Nanoparticles in the clinic, *Bioeng. Transl. Med.*, 2016, **1**(1), 10–29.
166 K. El-Boubbou, Magnetic iron oxide nanoparticles as drug carriers: clinical relevance, *Nanomedicine*, 2018, **13**(8), 953–971.
167 A. Wicki, *et al.*, Nanomedicine in cancer therapy: challenges, opportunities, and clinical applications, *J. Controlled Release*, 2015, **200**, 138–157.
168 J. Wolfram and M. Ferrari, Clinical cancer nanomedicine, *Nano Today*, 2019, (25), 85–98.
169 P. R. Gil, *et al.*, Nanopharmacy: Inorganic nanoscale devices as vectors and active compounds, *Pharmacol. Res.*, 2010, **62**(2), 115–125.
170 K. Mahmoudi, *et al.*, Magnetic hyperthermia therapy for the treatment of glioblastoma: a review of the therapy's history, efficacy and application in humans, *Int. J. Hyperthermia*, 2018, **34**(8), 1316–1328.
171 O. Grauer, *et al.*, Combined intracavitary thermotherapy with iron oxide nanoparticles and radiotherapy as local

treatment modality in recurrent glioblastoma patients, *J. Neuro-Oncol.*, 2019, **141**(1), 83–94.

172 A. C. Anselmo and S. Mitragotri, A review of clinical translation of inorganic nanoparticles, *AAPS J.*, 2015, **17**(5), 1041–1054.

173 J. Shi, *et al.*, Cancer nanomedicine: progress, challenges and opportunities, *Nat. Rev. Cancer*, 2017, **17**(1), 20.

174 S. J. Oldenburg, *et al.*, *Current Good Manufacturing Practices (cGMPs) in the Commercial Development of Nanomaterials for Hyperthermia Applications*, in *Nanomaterials for Magnetic and Optical Hyperthermia Applications*, Elsevier, 2019, pp. 339–353.

175 S. Bayda, *et al.*, Inorganic nanoparticles for cancer therapy: a transition from lab to clinic, *Curr. Med. Chem.*, 2018, **25**(34), 4269–4303.

176 C. Lee, *et al.*, Rabies virus-inspired silica-coated gold nanorods as a photothermal therapeutic platform for treating brain tumors, *Adv. Mater.*, 2017, **29**(13), 1605563.

177 H. Zhou, *et al.*, Dual targeting hyaluronic acid-RGD mesoporous silica coated gold nanorods for chemo-photothermal cancer therapy, *Mater. Sci. Eng., C*, 2017, **81**, 261–270.

178 J. Liu, *et al.*, Tumor acidity activating multifunctional nanoplatform for NIR-mediated multiple enhanced photodynamic and photothermal tumor therapy, *Biomaterials*, 2018, **157**, 107–124.

179 Z. Zhang, *et al.*, Silver nanoparticle gated, mesoporous silica coated gold nanorods (AuNR@ MS@ AgNPs): low premature release and multifunctional cancer theranostic platform, *ACS Appl. Mater. Interfaces*, 2015, **7**(11), 6211–6219.

180 G. F. Luo, *et al.*, A Triple-Collaborative Strategy for High-Performance Tumor Therapy by Multifunctional Mesoporous Silica-Coated Gold Nanorods, *Adv. Funct. Mater.*, 2016, **26**(24), 4339–4350.

181 S. Baek, *et al.*, Triple hit with drug carriers: pH-and temperature-responsive theranostics for multimodal chemo- and photothermal therapy and diagnostic applications, *ACS Appl. Mater. Interfaces*, 2016, **8**(14), 8967–8979.

182 C. Xu, *et al.*, Bacteria-like mesoporous silica-coated gold nanorods for positron emission tomography and photoacoustic imaging-guided chemo-photothermal combined therapy, *Biomaterials*, 2018, **165**, 56–65.

183 X. Li, *et al.*, Formation of gold nanostar-coated hollow mesoporous silica for tumor multimodality imaging and photothermal therapy, *ACS Appl. Mater. Interfaces*, 2017, **9**(7), 5817–5827.

184 Y. Gao, *et al.*, Multifunctional gold nanostar-based nanocomposite: synthesis and application for noninvasive MR-SERS imaging-guided photothermal ablation, *Biomaterials*, 2015, **60**, 31–41.

185 J. An, *et al.*, In Vivo Computed Tomography/Photoacoustic Imaging and NIR-Triggered Chemo–Photothermal Combined Therapy Based on a Gold Nanostar-, Mesoporous Silica-, and Thermosensitive Liposome-Composited Nanoprobe, *ACS Appl. Mater. Interfaces*, 2017, **9**(48), 41748–41759.

186 D. Li, *et al.*, Construction of polydopamine-coated gold nanostars for CT imaging and enhanced photothermal therapy of tumors: an innovative theranostic strategy, *J. Mater. Chem. B*, 2016, **4**(23), 4216–4226.

187 P. Wei, *et al.*, Dendrimer-Stabilized gold nanostars as a multifunctional theranostic nanoplatform for CT imaging, photothermal therapy, and gene silencing of tumors, *Adv. Healthcare Mater.*, 2016, **5**(24), 3203–3213.

188 Y. Liu, *et al.*, Gold nanoshell-based betulinic acid liposomes for synergistic chemo-photothermal therapy, *Nanomedicine*, 2017, **13**(6), 1891–1900.

189 U. SeokáChung, Dendrimer porphyrin-coated gold nanoshells for the synergistic combination of photodynamic and photothermal therapy, *Chem. Commun.*, 2016, **52**(6), 1258–1261.

190 C. Iodice, *et al.*, Enhancing photothermal cancer therapy by clustering gold nanoparticles into spherical polymeric nanoconstructs, *Opt. Lasers Eng.*, 2016, **76**, 74–81.

191 J. Yang, *et al.*, Spatially confined fabrication of core–shell gold nanocages@ mesoporous silica for near-infrared controlled photothermal drug release, *Chem. Mater.*, 2013, **25**(15), 3030–3037.

192 F. Hu, *et al.*, Double-Walled Au Nanocage/SiO2 nanorattles: integrating SERS imaging, drug delivery and photothermal therapy, *Small*, 2015, **11**(8), 985–993.

193 J. Hou, *et al.*, PEGylated (NH 4) x WO 3 nanorod mediated rapid photonecrosis of breast cancer cells, *Nanoscale*, 2019, **11**(21), 10209–10219.

194 L. Cheng, *et al.*, PEGylated WS2 nanosheets as a multifunctional theranostic agent for in vivo dual-modal CT/photoacoustic imaging guided photothermal therapy, *Adv. Mater.*, 2014, **26**(12), 1886–1893.

195 X. Jia, *et al.*, BSA-exfoliated WSe 2 nanosheets as a photoregulated carrier for synergistic photodynamic/photothermal therapy, *J. Mater. Chem. B*, 2017, **5**(2), 269–278.

196 Y. Yong, *et al.*, WS2 nanosheet as a new photosensitizer carrier for combined photodynamic and photothermal therapy of cancer cells, *Nanoscale*, 2014, **6**(17), 10394–10403.

197 Y. Yong, *et al.*, Tungsten sulfide quantum dots as multifunctional nanotheranostics for in vivo dual-modal image-guided photothermal/radiotherapy synergistic therapy, *ACS Nano*, 2015, **9**(12), 12451–12463.

198 Q. Zhang, *et al.*, The theranostic nanoagent Mo 2 C for multi-modal imaging-guided cancer synergistic phototherapy, *Biomater. Sci.*, 2019, **7**(7), 2729–2739.

199 J. Wu, *et al.*, Functionalized MoS2 nanosheet-capped periodic mesoporous organosilicas as a multifunctional platform for synergistic targeted chemo-photothermal therapy, *Chem. Eng. J.*, 2018, **342**, 90–102.

200 X. Li, *et al.*, Facile synthesis of soybean phospholipid-encapsulated MoS2 nanosheets for efficient in vitro and in vivo photothermal regression of breast tumor, *Int. J. Nanomed.*, 2016, **11**, 1819.

201 H. Zu, *et al.*, Rapid room-temperature preparation of MoO_{3-x} quantum dots by ultraviolet irradiation for photo-

thermal treatment and glucose detection, *New J. Chem.*, 2018, **42**(23), 18533–18540.

202 W. Dai, H. Dong and X. Zhang, A semimetal-like molybdenum carbide quantum dots photoacoustic imaging and photothermal agent with high photothermal conversion efficiency, *Materials*, 2018, **11**(9), 1776.

203 W. Feng, *et al.*, Flower-like PEGylated MoS 2 nanoflakes for near-infrared photothermal cancer therapy, *Sci. Rep.*, 2015, **5**, 17422.

204 L. Chen, *et al.*, One-pot synthesis of MoS2 nanoflakes with desirable degradability for photothermal cancer therapy, *ACS Appl. Mater. Interfaces*, 2017, **9**(20), 17347–17358.

205 T. Liu, *et al.*, Ultra-small MoS 2 nanodots with rapid body clearance for photothermal cancer therapy, *Nano Res.*, 2016, **9**(10), 3003–3017.

206 A. Zhang, *et al.*, An efficient and self-guided chemo-photothermal drug loading system based on copolymer and transferrin decorated MoS2 nanodots for dually controlled drug release, *Chem. Eng. J.*, 2018, **342**, 120–132.

207 F. Qi and R. Liu, Tumor-targeted and biocompatible MoSe 2 nanodots@ albumin nanospheres as a dual-modality therapy agent for synergistic photothermal radiotherapy, *Nanoscale Res. Lett.*, 2019, **14**(1), 67.

208 H. Peng, *et al.*, Highly Ligand-Directed and Size-Dependent Photothermal Properties of Magnetite Particles, *Part. Part. Syst. Charact.*, 2016, **33**(6), 332–340.

209 Z. Zhou, *et al.*, Iron/iron oxide core/shell nanoparticles for magnetic targeting MRI and near-infrared photothermal therapy, *Biomaterials*, 2014, **35**(26), 7470–7478.

210 H. Chen, *et al.*, Highly crystallized iron oxide nanoparticles as effective and biodegradable mediators for photothermal cancer therapy, *J. Mater. Chem. B*, 2014, **2**(7), 757–765.

211 S. Shen, *et al.*, CMCTS stabilized Fe 3 O 4 particles with extremely low toxicity as highly efficient near-infrared photothermal agents for in vivo tumor ablation, *Nanoscale*, 2013, **5**(17), 8056–8066.

212 R. Zheng, *et al.*, Polydopamine-coated magnetic composite particles with an enhanced photothermal effect, *ACS Appl. Mater. Interfaces*, 2015, **7**(29), 15876–15884.

213 S. Shen, *et al.*, Magnetic nanoparticle clusters for photothermal therapy with near-infrared irradiation, *Biomaterials*, 2015, **39**, 67–74.

214 S. Bhana, *et al.*, Near-infrared-absorbing gold nanopopcorns with iron oxide cluster core for magnetically amplified photothermal and photodynamic cancer therapy, *ACS Appl. Mater. Interfaces*, 2015, **7**(21), 11637–11647.

215 A. Espinosa, *et al.*, Duality of iron oxide nanoparticles in cancer therapy: amplification of heating efficiency by magnetic hyperthermia and photothermal bimodal treatment, *ACS Nano*, 2016, **10**(2), 2436–2446.

216 X. Yi, *et al.*, Imaging-Guided Combined Photothermal and Radiotherapy to Treat Subcutaneous and Metastatic Tumors Using Iodine-131-Doped Copper Sulfide Nanoparticles, *Adv. Funct. Mater.*, 2015, **25**(29), 4689–4699.

217 Y. Huang, *et al.*, Copper Sulfide Nanoparticles with Phospholipid-PEG Coating for In Vivo Near-Infrared Photothermal Cancer Therapy, *Chem. – Asian J.*, 2015, **10**(2), 370–376.

218 S. Zhang, *et al.*, Ambient aqueous synthesis of ultrasmall PEGylated $Cu_{2-x}Se$ nanoparticles as a multifunctional theranostic agent for multimodal imaging guided photothermal therapy of cancer, *Adv. Mater.*, 2016, **28**(40), 8927–8936.

219 Q. Tian, *et al.*, Hydrophilic Cu9S5 nanocrystals: a photothermal agent with a 25.7% heat conversion efficiency for photothermal ablation of cancer cells in vivo, *ACS Nano*, 2011, **5**(12), 9761–9771.

220 S. Wang, *et al.*, Plasmonic copper sulfide nanocrystals exhibiting near-infrared photothermal and photodynamic therapeutic effects, *ACS Nano*, 2015, **9**(2), 1788–1800.

221 K.-C. Li, *et al.*, PEGylated copper nanowires as a novel photothermal therapy agent, *ACS Appl. Mater. Interfaces*, 2016, **8**(19), 12082–12090.

222 J. Mou, *et al.*, Ultrasmall Cu2-xS Nanodots for Highly Efficient Photoacoustic Imaging-Guided Photothermal Therapy, *Small*, 2015, **11**(19), 2275–2283.

223 M. Zhou, *et al.*, CuS nanodots with ultrahigh efficient renal clearance for positron emission tomography imaging and image-guided photothermal therapy, *ACS Nano*, 2015, **9**(7), 7085–7096.

224 W. Feng, *et al.*, In vitro and in vivo toxicity studies of copper sulfide nanoplates for potential photothermal applications, *Nanomedicine*, 2015, **11**(4), 901–912.

225 M. Nurunnabi, *et al.*, Photoluminescent graphene nanoparticles for cancer phototherapy and imaging, *ACS Appl. Mater. Interfaces*, 2014, **6**(15), 12413–12421.

226 Y. Liu, *et al.*, Gold-nanobranched-shell based drug vehicles with ultrahigh photothermal efficiency for chemo-photothermal therapy, *Nanomedicine*, 2019, **18**, 303–314.

227 S. Y. Lee, C. L. Peng and M. J. Shieh, Combined Chemo-Photothermotherapy Using Gold Nanoshells on Drug-Loaded Micellar Templates for Colorectal Cancer Treatment, *Part. Part. Syst. Charact.*, 2018, **35**(12), 1800334.

228 J. Peng, *et al.*, Mesoporous magnetic gold "nanoclusters" as theranostic carrier for chemo-photothermal co-therapy of breast cancer, *Theranostics*, 2014, **4**(7), 678.

229 P. Liu, *et al.*, Concurrent photothermal therapy and photodynamic therapy for cutaneous squamous cell carcinoma by gold nanoclusters under a single NIR laser irradiation, *J. Mater. Chem. B*, 2019, **7**(44), 6924–6933.

230 S. Huang, *et al.*, A54 peptide-mediated functionalized gold nanocages for targeted delivery of DOX as a combinational photothermal-chemotherapy for liver cancer, *Int. J. Nanomed.*, 2017, **12**, 5163.

231 J.-G. Piao, *et al.*, pH-sensitive zwitterionic coating of gold nanocages improves tumor targeting and photothermal treatment efficacy, *Nano Res.*, 2018, **11**(6), 3193–3204.